

Odd-parity quadrupole order and induced nonreciprocal transport in kagome metal CsTi_3Bi_5 driven by quantum interference mechanism

Jianxin Huang¹, Youichi Yamakawa¹, Rina Tazai², Takahiro Morimoto³ and Hiroshi Kontani¹

¹*Department of Physics, Nagoya University, Nagoya 464-8602, Japan*

²*Yukawa Institute for Theoretical Physics, Kyoto University, Kyoto 606-8502, Japan*

³*Department of Applied Physics, The University of Tokyo, Tokyo 113-8656, Japan*

(Dated: February 27, 2024)

Kagome metals present a fascinating platform of novel quantum phases thanks to the interplay between the geometric frustration and strong electron correlation. Here, we propose the emergence of the electric toroidal quadrupole order that originates from the intra-unit-cell odd-parity configuration in recently discovered kagome metal CsTi_3Bi_5 . The predicted E_{1u} bond-order is induced by the beyond-mean-field mechanism, that is, the quantum interference among different sublattice spin fluctuations. Importantly, the accompanied nematic deformation of the Fermi surface is just $\sim 1\%$ while the intensity of the quasiparticle interference signal exhibits drastic nematic anisotropy, consistently with the scanning tunneling microscope measurements in CsTi_3Bi_5 . The present odd-parity quadrupole order triggers interesting phenomena, such as the non-linear Hall effect and emergent electromagnetism.

Introduction.— The discovery of kagome metals has greatly enriched the study of condensed matter physics. The interplay between the geometric frustration and strong electron correlation gives rise to novel quantum phases. For instance, the 2×2 charge-density-wave (CDW) order [1–4], the time-reversal-symmetry (TRS) breaking loop-current order [5–9], the nematic order [4, 10, 11], and superconductivity [12, 13], have been discovered in the V-based kagome metal AV_3Sb_5 (A=Cs,Rb,K). Similar quantum phase transitions (such as the $\sqrt{3} \times \sqrt{3}$ CDW without the TRS) are observed in bilayer kagome metal ScV_6Sn_6 [14]. Various theoretical studies have been conducted on the origin of quantum states in kagome metals [15–24], by focusing on the strong correlation and geometric frustration. However, numerous essential electronic properties remain unresolved.

The recent discovery of a Ti-based kagome superconductor CsTi_3Bi_5 [24–31] has revealed that further exotic electronic states emerge. While no CDW occurs that breaks translational symmetry, CsTi_3Bi_5 exhibits quantum phases similar to V-based Kagome metals, such as the nematicity and superconductivity ($T_c = 4.8\text{K}$). The nematic order has been revealed by the scanning tunneling microscope (STM) measurements [28, 29], and its transition temperature is $T_0 \sim 100\text{K}$ according to the angular-dependent magnetoresistance [29]. The wavevector of the order parameter is $\mathbf{q} = \mathbf{0}$ because of no Fermi surface (FS) reconstruction [28, 29]. Notably, however, the nematicity in CsTi_3Bi_5 has characteristic properties that would be distinct from other nematic metals. Also, the lattice deformation and the kink in the resistivity at $T \sim T_0$ is almost invisible. For $T \ll T_0$, in contrast, small nematic deformation of the FS leads to the drastic anisotropic quasiparticle (QP) scattering. These facts indicate the emergence of a novel quantum state in Ti-based kagome metals.

Importantly, the electronic nematic order ($\mathbf{q} = \mathbf{0}$) tran-

scends the realm of the mean-field (or classical) order, where the FS nesting ($\mathbf{q} \neq \mathbf{0}$) leads the kinetic energy gain. That is, the nematicity without band folding is a hallmark of the nontrivial quantum correlations. A famous example is Fe-based SCs, where the nematic order with the orbital polarization is caused by the beyond-mean-field electron correlations [32–41]. In FeSe family, the nematic QCP gives the critical behaviors and pairing mechanism [42]. In contrast, in Ti-based kagome metals, the “onsite orbital degeneracy” is absent, and the induced anomalies in the resistivity and the lattice constant are quite small. Therefore, the origin of unusual nematicity in Ti-based kagome metal and its relation to other nematic metals are highly nontrivial.

In this paper, we find that the E_{1u} symmetry bond-order (BO) is induced by the inter-sublattice attraction due to the paramagnon interference mechanism. Here, intra-unit-cell staggered BO leads to the nonpolar odd-parity state (*i.e.*, electric toroidal quadrupole BO), which has rarely been studied in strongly correlated metals. The E_{1u} BO explains the almost invisible anomalies in the resistivity and the lattice constant at $T \lesssim T_0$ because $\Delta k_F \propto \phi^2$ ($\propto T_0 - T$). For $T \ll T_0$, however, large E_{1u} BO ($\phi \gg T_0$) causes the remarkable nematic QP interference (QPI) signal observed in CsTi_3Bi_5 [28, 29]. Interestingly, we reveal that the odd-parity E_{1u} BO triggers nonreciprocal non-linear Hall (NLH) effect.

Model Hamiltonian.— The two-dimensional kagome lattice structure of CsTi_3Bi_5 is shown in Fig. 1 (a). Each unit-cell is composed of three Ti-ion sublattices A, B, C. We derive the 30 orbital tight-binding model with 15 Ti d -orbitals and 15 Bi p -orbitals based on the bandstructure given by the WIEN2k software, which is shown in the Supplemental Materials (SM) A [43]. The d -electron FSs are mainly composed of the xy orbital in addition to xz orbital. ($N_{xz}(0) \sim 0.4N_{xy}(0)$ as shown in Fig. S1 (c) [43].) The number of electrons in Ti-based system per

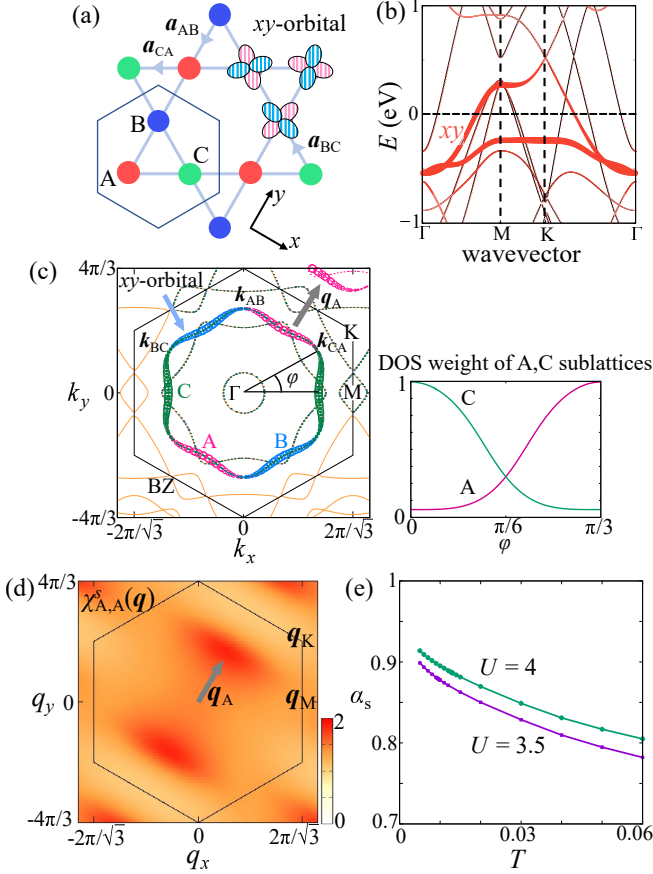


FIG. 1. (a) Kagome lattice structure composed of Ti ions. The unit cell contains three sublattices A (red), B (blue), and C (green). (b) Bandstructure of CsTi₃Bi₅ model. (c) FSs of CsTi₃Bi₅ model. The *xy* orbital weight of A, B, and C sublattices are depicted by red, blue and green colors, respectively. The sublattice DOS on the *xy*-orbital FS is shown. (d) Spin susceptibility $\chi_{A,A}^s(\mathbf{q})$ for $U = 4$ at $T = 0.01$. (e) Stoner factor α_S for $U = 4$ and 3.5 as function of T .

Ti ion is one less than in the V-based system, leading to smaller FSs with different *d*-orbital character. Notably, the van-Hove singularity (vHS) points, which play an important role in V-based systems, are far away from the Fermi level in the Ti-based system. The bandstructure of the 30 orbital model is shown in Fig. 1 (b).

Figure 1 (c) shows the FS of the present two-dimensional model, which well reproduce the ARPES measurement [24]. The *xy* orbital weight of A, B, and C sublattices are depicted by red, blue and green colors, respectively. (The inset shows the sublattice density-of-states (DOS) on the *xy*-orbital FS.) There is a prominent intra-sublattice nesting at $\mathbf{q} = \mathbf{q}_A$, in highly contrast to the absence of the intra-sublattice nesting in the “pure-type FS” of V-based kagome metals (called the “sublattice interference”) [15, 18]. The DOS at the Fermi level is mainly composed of the *xy* orbital, and we verified that the spin fluctuations develop only in the *xy*-orbital based on the multiorbital random-phase approximation

(RPA), as we explain in the SM A [43]. Therefore, we introduce the Coulomb interaction only on the *xy*-orbital in the present study. Hereafter, the unit of the energy is eV unless otherwise noted.

Spin Susceptibility and Self-Energy.— Here, we calculate the spin susceptibility $\chi_{l,m}^s(\mathbf{q})$ self-consistently by including the spin fluctuation induced self-energy $\Sigma_{l,m}(k)$ of the *xy*-orbital electrons. Here, $k \equiv (\mathbf{k}, \epsilon_n = (2n + 1)\pi T)$ and $l, m = A, B, C$. We use the fluctuation-exchange (FLEX) approximation [44–46], which is explained in the SM B [43]. The obtained spin susceptibility $\chi_{A,A}^s(\mathbf{q})$ for $U = 4$ at $T = 0.01$ is shown in Fig. 1 (d). Due to the geometrical frustration, $\chi_{A,A}^s(\mathbf{q})$ exhibits a very broad peak around the nesting vector \mathbf{q}_A in Fig. 1 (c), which is favorable for the “paramagnon interference mechanism” given by the convolution of two χ^s s (see Fig. 2 (a)). Note that $\chi_{l,m}^s(\mathbf{q})$ is small for $l \neq m$, meaning that the spin susceptibility is “sublattice selective”. Figure 1 (e) shows the Stoner factor $\alpha_S \equiv \max_{\mathbf{q}} U \chi^s(\mathbf{q})$. Magnetism appears when $\alpha_S \geq 1$. Thus, the systems remains paramagnetic till low temperatures owing to the geometrical frustration.

Linearized DW Equation.— The nonlocal nature of the BO states is not obtained in the FLEX approximation. However, the BO can be induced by the beyond-FLEX nonlocal correlations, called the vertex corrections (VCs) [32–34, 40]. The BO due to the VCs are derived from the linearized DW equation [40]:

$$\lambda_{\mathbf{q}} f_{\mathbf{q}}^L(k) = -\frac{T}{N} \sum_{p, M_1, M_2} I_{\mathbf{q}}^{L, M_1}(k, p) \times \{G(p)G(p + \mathbf{q})\}^{M_1, M_2} f_{\mathbf{q}}^{M_2}(p), \quad (1)$$

where $L \equiv (l, l')$ and $M_i \equiv (m_i, m'_i)$ represent the pair of sublattices A, B, C. $I_{\mathbf{q}}^{L, M}(k, p)$ is the “electron-hole pairing interaction”. It is uniquely derived from the functional derivative of the FLEX self-energy to satisfy the conserving laws: $I_{\mathbf{q}=0}^{L, M}(k, p) = \delta \Sigma_L(k) / \delta G_M(p)$ [47]. $\lambda_{\mathbf{q}}$ is the eigenvalue that represents the instability of the DW at wavevector \mathbf{q} , and $\max_{\mathbf{q}} \{\lambda_{\mathbf{q}}\} = 1$ at $T = T_0$. Hereafter, the form factor is normalized as $\max_{l, m, \mathbf{k}} |f_{\mathbf{q}}^{l, m}(\mathbf{k})| = 1$. The physical meaning of the form factor and the derivation of the DW equation based on the Luttinger-Ward theory are given in the SM C and SM D, respectively [43].

$f_{\mathbf{q}}^L(k)$ is the Hermite form factor that is proportional to the particle-hole (p-h) condensation $\sum_{\sigma} \{ \langle c_{\mathbf{k}+\mathbf{q}, l, \sigma}^{\dagger} c_{\mathbf{k}, l', \sigma} \rangle - \langle \cdots \rangle_0 \}$, or equivalently, the symmetry breaking component in the self-energy. The kernel function I in Eq. (1) contains the Aslamazov-Larkin (AL) terms shown in Figs. 2 (a) and (b). Importantly, the interference between two-paramagnons gives rise to the charge-channel DW at $\mathbf{q}_{\text{BO}} = \mathbf{0}$ constructively; see the SM B [43] for detail. In FeSe, the AL terms drive the nonmagnetic nematic order [32]. The importance of AL terms was verified by the functional-renormalization-

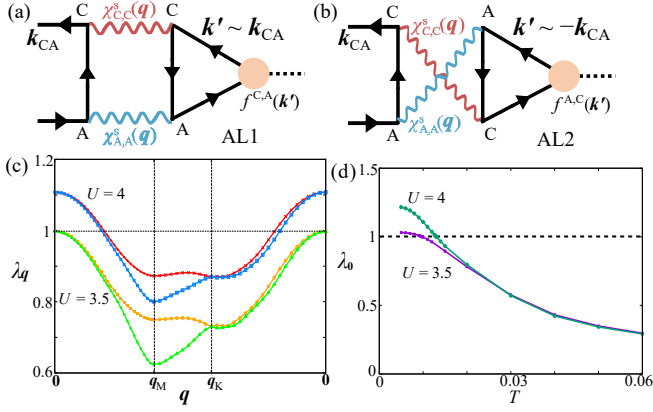


FIG. 2. (a) AL1 and (b) AL2 processes that give the BO at $\mathbf{q}_{BO} = \mathbf{0}$. Note that $f^{A,C}(-\mathbf{k}) = -f^{A,C}(\mathbf{k}) = f^{C,A}(\mathbf{k})$ in the E_{1u} state. (c) \mathbf{q} -dependence of the largest and the second largest eigenvalues for $U = 4$ and 3.5. \mathbf{q}_M and \mathbf{q}_K are shown in Fig. 1 (d). (d) T -dependence of the largest λ_q at $\mathbf{q} = \mathbf{0}$.

group (fRG) study for several Hubbard models, in which higher-order VCs are generated in an unbiased way [35–37]. The AL terms originate from the spin-fluctuation-induced reduction in the free-energy promoted by the BO; see the SM D [43].

Here, we solve the charge-channel DW equation (1). As shown in Fig. 2 (c), the eigenvalue takes the maximum at $\mathbf{q} = \mathbf{0}$ in Ti-based kagome metal for both $U = 4$ and 3.5 at $T = 0.01$. As we will explain below, the obtained doubly-degenerate eigenvalues at $\mathbf{q} = \mathbf{0}$ gives the odd-parity E_{1u} BO, which gives the nematic FS deformation as shown in the SM E [43]. The T -dependence of $\lambda_{\mathbf{q}=\mathbf{0}}$ is shown in Fig. 2 (d). The transition temperature is $T_0 \approx 0.013$ for $U = 4$. Note that the even-parity E_{2g} symmetry BO gives the second largest instability; see Figs. S8 and S9 in the SM F [43].

In the SM D [43], we derive the order parameter under the E_{1u} BO transition temperature by solving the “full DW equation”. The obtained $\phi(T)$ naturally explain the nematic anisotropy reported in CsTi_3Bi_5 [28, 29], as we discuss in the SM G [43].

Odd-parity E_{1u} BO solution.— Here, we analyze the symmetry of the obtained form factor. Figure 3 (a) exhibits one of the doubly-degenerate form factors at $\mathbf{q} = \mathbf{0}$, $f^{B,C}(\mathbf{k})$ and $f^{C,A}(\mathbf{k})$, for $U = 4$ at $T = 0.01$. The obtained $f^{l,m}(\mathbf{k})$ is pure imaginary and odd-parity with respect to $\mathbf{k} \rightarrow -\mathbf{k}$ ($f^{l,m}(\mathbf{k}) = -f^{l,m}(-\mathbf{k})$) and $l \leftrightarrow m$ ($f^{l,m}(\mathbf{k}) = -f^{m,l}(\mathbf{k})$). Note that $f_{CA}(\mathbf{k}) \propto i \sin \mathbf{k} \cdot \mathbf{a}_{CA}$. Its BO in real-space is $\delta t_{i,j} \propto \sum_{\mathbf{k}} f^{l,m}(\mathbf{k}) e^{i\mathbf{k} \cdot (\mathbf{r}_i - \mathbf{r}_j)}$, which is real and even-parity $\delta t_{i,j} = \delta t_{j,i}$. Note that i (j) is the site index of sublattice l (m). Figure 3 (b) depicts the bond-order in real space derived from the Fourier transform of the form factor in Fig. 3 (a). Its orthogonal state is shown in Fig. 3 (c). The parity of the mirror operation $M_{x(y)}$, $x(y) \rightarrow -x(-y)$, is shown by its superscript (\pm) in Figs. 3 (b) and (c). Thus,

the parity of the inversion is $I = M_x M_y = -1$ (=odd-parity). In addition, this is not a ferroelectric metal. Apparently, the nonpolar odd-parity originates from the intra-unit-cell staggered BO, which is called the electric toroidal quadrupole (ETQ) BO. It is rarely studied in strongly correlated metals. Note that the ETQ state in pyrochlore metal $\text{Cd}_2\text{Re}_2\text{O}_7$ [49–52] is considered to be closely tied to the strong spin-orbit interaction (SOC), while the SOC is unnecessary in the present mechanism for Ti-kagome.

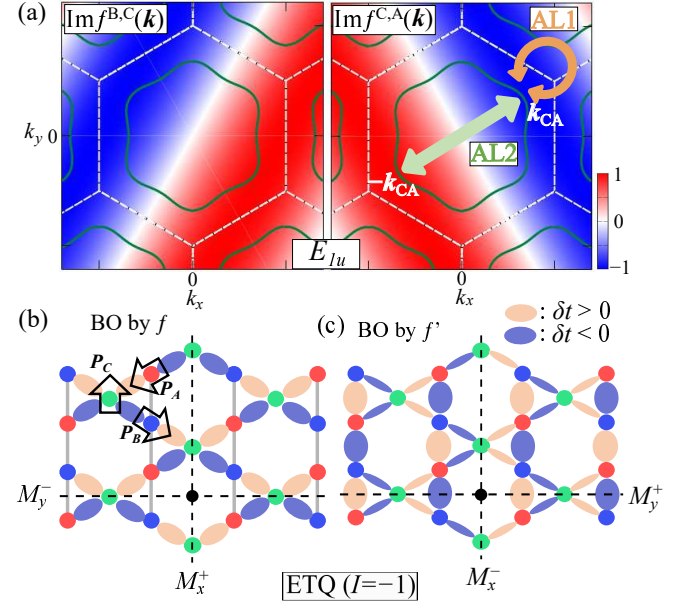


FIG. 3. (a) Odd-parity form factors $\text{Im} f^{B,C}(\mathbf{k})$ and $\text{Im} f^{C,A}(\mathbf{k})$ at wavevector $\mathbf{q} = \mathbf{0}$. (Note that $\text{Im} f^{B,C}(\mathbf{k}) \propto i \sin \mathbf{k} \cdot \mathbf{a}_{BC}$ is periodic in the extended BZ.) The original xy -orbital FS is shown in each panel. (b) E_{1u} BO (=modulation of the hopping integrals) in real space derived from the form factor $\hat{f}(\mathbf{k})$ in (a). The parity of $M_{x(y)}$ operation is shown by its superscript (\pm). The electric dipole at each sublattice \mathbf{P}_l cancels in total. (c) E_{1u} BO in real space derived from \hat{f}' , which is orthogonal to \hat{f} .

Now, we explain why E_{1u} BO is caused by the AL terms in Figs. 2 (a) and (b), which give the l.h.s of the DW equation $\lambda_{\mathbf{q}=\mathbf{0}} f^{C,A}(\mathbf{k})$. In this model, $\chi_{l,m}^s$ are large for $l = m$ (i.e., sublattice selective), and the AL1 term in Fig. 2 (a) [AL2 term in (b)] gives the attraction between \mathbf{k} and $\mathbf{k}' \approx \mathbf{k}$ [$\mathbf{k}' \approx -\mathbf{k}$] due to the particle-particle [particle-hole] process included in AL1 [AL2] [48]. By setting $\mathbf{k} = \mathbf{k}_{CA}$ shown in Fig. 1 (c), we obtain

$$[\text{AL1}]^{C,A}(\mathbf{k}_{CA}) \sim I_{AL} N(0) f^{C,A}(\mathbf{k}_{CA}), \quad (2)$$

$$[\text{AL2}]^{C,A}(\mathbf{k}_{CA}) \sim I_{AL} N(0) f^{A,C}(-\mathbf{k}_{CA}), \quad (3)$$

where $I_{AL} > 0$ is the attraction and $N(0)$ is the xy -orbital DOS per sublattice. Because $f^{A,C}(-\mathbf{k}_{CA}) = -\{f^{C,A}(\mathbf{k}_{CA})\}^* = f^{C,A}(\mathbf{k}_{CA})$, [AL1] and [AL2] cooperatively contribute to the odd-parity BO shown in Fig. 3

(a). (Here, the sublattice degrees of freedom is essential because AL1 and AL2 cancel for the “intra-sublattice” odd-parity BO; $f^{l,l}(\mathbf{k}) = -f^{l,l}(\mathbf{k})$.) The attractions work between the two points of the orange arrow (by AL1) and the green arrow (by AL2). Note that the inter-sublattice form factor $f^{l,m}(\mathbf{k})$ ($l \neq m$) is not periodic in the 1st BZ due to the extra phase factor $e^{i\mathbf{k}\cdot(\mathbf{r}_l - \mathbf{r}_m)}$. The E_{1u} BO in real space are shown in Figs. 3 (b) and (c). Each E_{1u} BO changes its sign by the inversion operation.

Interestingly, the quantum interference mechanism explains both the odd-parity BO in Ti-based kagome metal and the 2×2 even-parity BO in V-based one [18] on the same footing; see the SM H [43]. The present electron-correlation mechanism is distinguishable from the electron-lattice coupling mechanism of polar metal transition that accompanies large lattice distortion [53].

Nematicity of Physical Quantities. — Since the solution for $\mathbf{q} = \mathbf{0}$ is doubly degenerate, there exists another form factor \hat{f}' orthogonal to \hat{f} , and (f, f') belongs to the E_{1u} representation. Each \hat{f} and \hat{f}' satisfies the Hermitian condition $f^{lm}(\mathbf{k}) = \{f^{ml}(\mathbf{k})\}^*$. Then, any linear combination $\hat{f}_\theta \equiv \hat{f} \cos \theta + \hat{f}' \sin \theta$ gives the solution of Eq. (1) without changing the eigenvalue. (The coefficients should be real to satisfy the Hermitian condition of $\hat{f}_\theta(\mathbf{k})$.) To see the FS deformation, we introduce the symmetry breaking self-energy due to the BO state as $\delta t_{\mathbf{k}}^\theta = \phi \hat{f}_\theta(\mathbf{k})$. (Apparently, $\max_{l,m,\mathbf{k}} |\delta t_{\mathbf{k}}^{l,m}| = \phi$.) The FSs derived from the eigenvalues of $\hat{h}_{\mathbf{k}}^0 + \delta t_{\mathbf{k}}^{\theta=0}$, where $\hat{h}_{\mathbf{k}}^0$ is the tight-binding model, for $\phi = 0 \sim 0.3$ are shown in Fig. 4 (a). (The director of the nematic FS is parallel to $(\cos \theta, \sin \theta)$; see SM E [43].) The FS deformation due to the E_{1u} BO is tiny for $\phi \lesssim 0.1$ because it is proportional to ϕ^2 , while it becomes comparable to experimental nematicity as shown in Fig. 4 (a).

Figure 4 (b) shows the nematic QPI signal given by the E_{1u} BO \hat{f} . Details of the numerical study are found in the SM G [43]. The obtained remarkable nematic QPI with large signal around \mathbf{q}_4 is quantitatively consistent with experiments. Importantly, $\phi \gtrsim 0.2$ is obtained in the full-DW equation analysis in the SM D [43]. In the ARPES measurement, ϕ and the bandwidth are renormalized by $z = m/m^* \sim 0.25$. Note that the nematic order in FeSe ($T_0 = 90\text{K}$) is $\phi^* \equiv z\phi \approx 50\text{meV}$ and $z \sim 0.25$ [54].

Non-linear Hall effect due to odd-parity BO. — Here, we discuss the NLH effect as an emergent phenomenon due to the odd-parity BO. This effect attracts great attention as nontrivial nonreciprocal transport in the TRS state driven by the Berry curvature dipole (BCD) [55]. The NLH effect has been recently observed in various metals with noncentrosymmetric crystal structures, such as transition metal dichalcogenides [56], twisted bilayer graphene [57], and Weyl semimetals [58]. However, the NLH effect driven by odd-parity quantum orders has rarely been studied so far. The NLH current due to the

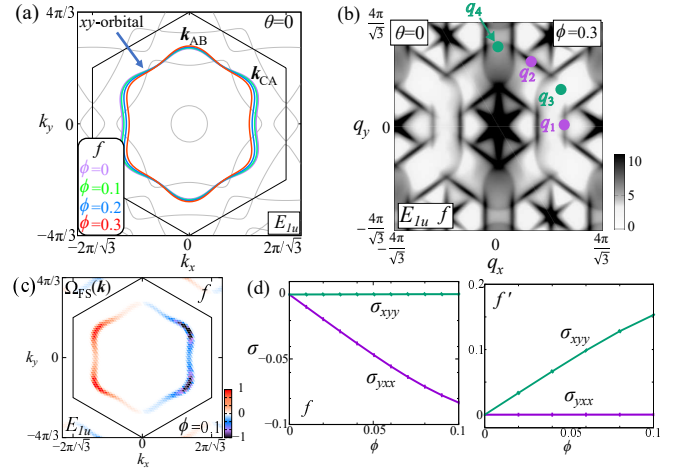


FIG. 4. (a) Nematic FS and (b) nematic QPI signal induced by the E_{1u} BO $\delta t_{\mathbf{k}}^{\theta=0} = \phi \hat{f}_{\theta=0}(\mathbf{k})$ for $\phi = 0.3$. $\mathbf{q}_1 \sim \mathbf{q}_4$ are the typical QPI momenta shown in Fig. S10 (e). Note that $\mathbf{q}_i \approx 2\mathbf{k}_i$, where \mathbf{k}_i is the Fermi momentum shown in Fig. S10 (a). (c) $\Omega_{\text{FS}}(\mathbf{k})$ under E_{1u} BO $\hat{f}(\mathbf{k})$. (d) NLH conductivity induced by the E_{1u} BO due to $\hat{f}(\mathbf{k})$ and $\hat{f}'(\mathbf{k})$ at $T = 0.01$.

BCD is $j_\alpha = \sigma_{\alpha\beta\beta} E_\beta^2$, and the relation $\sigma_{xyy} = -\sigma_{yxy}$ holds. The NLH conductivity $\sigma_{\alpha\beta\beta}$ is given as [55]

$$\sigma_{\alpha\beta\beta} = \varepsilon_{\alpha\beta z} e^3 \tau \frac{1}{N} \sum_{b,\mathbf{k}} f(\epsilon_{b,\mathbf{k}}) \partial_\beta \Omega(b, \mathbf{k}) \quad (4)$$

where $\alpha, \beta = x$ or y , $f(E)b = (e^{(E-\mu)/T} + 1)^{-1}$, and τ is the conduction electron relaxation time. $\Omega(b, \mathbf{k}) = i(\langle \partial_x u_{\mathbf{k}}^b | \partial_y u_{\mathbf{k}}^b \rangle - (x \leftrightarrow y))$, where $\partial_\nu \equiv \partial / \partial k_\nu$ ($\nu = x, y$) and $u_{\mathbf{k}}^b$ is the Bloch wavefunction for the b th band. When the inversion symmetry is broken, the Berry curvature is an odd function of \mathbf{k} ($\Omega(b, \mathbf{k}) = -\Omega(b, -\mathbf{k})$) in the TRS state [55]. Here, we find that the E_{1u} BO actually induces the finite NLH effect due to the BCD. Importantly, the present NLH effect occurs even without the SOC.

Figure 4 (c) shows the Berry curvature on the FS, $\Omega_{\text{FS}}(\mathbf{k}) = \sum_b f'(\epsilon_{b,\mathbf{k}}) \Omega(b, \mathbf{k})$ under the E_{1u} BO due to $\hat{f}_{\theta=0}$. The BCD along k_y axis originates from the mirror symmetry violation with respect to $y \rightarrow -y$. The NLH conductivity $\sigma_{\alpha\beta\beta}$ induced by $\hat{f}_{\theta=0}$ BO is shown in Fig. 4 (d). Here, σ_{xyy} is ϕ -linear, while $\sigma_{yxx} = 0$. (Here, we set $\tau = 1$ for simplicity.) We also show the NLH conductivity due to $\hat{f}_{\theta=\pi/2}$ BO. We stress that the NLH effect in CsTi_3Bi_5 originates from the quantum phase transition, in highly contrast to the NLH effect in noncentrosymmetric lattice [58, 59].

In addition, the inversion symmetry violation due to the E_{1u} BO will be observed by the second-harmonic generation [52]. Furthermore, the E_{1u} BO will give rise to the “antisymmetric SOC” by taking the atomic Ti and Bi SOC, which will trigger interesting emergent electromagnetism like the Edelstein effect [60].

Summary. — We predict the emergence of the E_{1u} sym-

metry ETQ BO, which has seldom been discussed so far, in CsTi_3Bi_5 . The emergent phenomena by the E_{1u} BO are very different from those by conventional even-parity BO (like the orbital order in FeSe): The E_{1u} BO explains the almost invisible anomalies in the resistivity and the lattice constant at $T \lesssim T_0$ because $\Delta k_F \propto \phi^2$. For $T \ll T_0$, however, large E_{1u} BO ($\phi \gg T_0$) causes the drastic nematic QPI signal observed in CsTi_3Bi_5 [28, 29] as discussed in the SM G [43]. Furthermore, we reveal that the E_{1u} BO triggers the quantum NLH effect.

This study has been supported by Grants-in-Aid for Scientific Research from MEXT of Japan (JP18H01175, JP20K03858, JP20K22328, JP22K14003, 23H01119), and by the Quantum Liquid Crystal No. JP19H05825 KAKENHI on Innovative Areas from JSPS of Japan.

-
- [1] B. R. Ortiz, L. C. Gomes, J. R. Morey, M. Winiarski, M. Bordelon, J. S. Mangum, I. W. H. Oswald, J. A. Rodriguez-Rivera, J. R. Neilson, S. D. Wilson, E. Ertekin, T. M. McQueen, and E. S. Toberer, *New kagome prototype materials: discovery of KV_3Sb_5 , RbV_3Sb_5 , and CsV_3Sb_5* , Phys. Rev. Materials **3**, 094407 (2019).
- [2] B. R. Ortiz, S. M. L. Teicher, Y. Hu, J. L. Zuo, P. M. Sarte, E. C. Schueller, A. M. M. Abeykoon, M. J. Krogstad, S. Rosenkranz, R. Osborn, R. Seshadri, L. Balents, J. He, and S. D. Wilson, *CsV_3Sb_5 : A Z_2 Topological Kagome Metal with a Superconducting Ground State*, Phys. Rev. Lett. **125**, 247002 (2020).
- [3] Y.-X. Jiang, J.-X. Yin, M. M. Denner, N. Shumiya, B. R. Ortiz, G. Xu, Z. Guguchia, J. He, M. S. Hossain, X. Liu, J. Ruff, L. Kautzsch, S. S. Zhang, G. Chang, I. Belopolski, Q. Zhang, T. A. Cochran, D. Multer, M. Litskevich, Z.-J. Cheng, X. P. Yang, Z. Wang, R. Thomale, T. Neupert, S. D. Wilson, and M. Z. Hasan, *Unconventional chiral charge order in kagome superconductor KV_3Sb_5* , Nat. Mater. **20**, 1353–1357 (2021).
- [4] H. Li, H. Zhao, B. R. Ortiz, T. Park, M. Ye, L. Balents, Z. Wang, S. D. Wilson, and I. Zeljkovic, *Rotation symmetry breaking in the normal state of a kagome superconductor KV_3Sb_5* , Nat. Phys. **18**, 265–270 (2022).
- [5] L. Yu, C. Wang, Y. Zhang, M. Sander, S. Ni, Z. Lu, S. Ma, Z. Wang, Z. Zhao, H. Chen, K. Jiang, Y. Zhang, H. Yang, F. Zhou, X. Dong, S. L. Johnson, M. J. Graf, J. Hu, H.-J. Gao, and Z. Zhao, *Evidence of a hidden flux phase in the topological kagome metal CsV_3Sb_5* , arXiv:2107.10714 (available at <https://arxiv.org/abs/2107.10714>).
- [6] C. Mielke, D. Das, J.-X. Yin, H. Liu, R. Gupta, Y.-X. Jiang, M. Medarde, X. Wu, H. C. Lei, J. Chang, P. Dai, Q. Si, H. Miao, R. Thomale, T. Neupert, Y. Shi, R. Khasanov, M. Z. Hasan, H. Luetkens, and Z. Guguchia, *Time-reversal symmetry-breaking charge order in a kagome superconductor*, Nature **602**, 245–250 (2022).
- [7] R. Khasanov, D. Das, R. Gupta, C. Mielke, M. Elender, Q. Yin, Z. Tu, C. Gong, H. Lei, E. T. Ritz, R. M. Fernandes, T. Birol, Z. Guguchia, and H. Luetkens, *Time-reversal symmetry broken by charge order in CsV_3Sb_5* , Phys. Rev. Research **4**, 023244 (2022).
- [8] Z. Guguchia, C. Mielke, D. Das, R. Gupta, J.-X. Yin, H. Liu, Q. Yin, M. H. Christensen, Z. Tu, C. Gong, N. Shumiya, M. S. Hossain, T. Gamsakhurdashvili, M. Elender, P. Dai, A. Amato, Y. Shi, H. C. Lei, R. M. Fernandes, M. Z. Hasan, H. Luetkens, and R. Khasanov, *Tunable unconventional kagome superconductivity in charge ordered RbV_3Sb_5 and KV_3Sb_5* , Nat. Commun. **14**, 153 (2023).
- [9] C. Guo, C. Putzke, S. Konyzheva, X. Huang, M. Gutierrez-Amigo, I. Errea, D. Chen, M. G. Vergniory, C. Felser, M. H. Fischer, T. Neupert, and P. J. W. Moll, *Switchable chiral transport in charge-ordered kagome metal CsV_3Sb_5* , Nature **611**, 461–466 (2022).
- [10] L. Nie, K. Sun, W. Ma, D. Song, L. Zheng, Z. Liang, P. Wu, F. Yu, J. Li, M. Shan, D. Zhao, S. Li, B. Kang, Z. Wu, Y. Zhou, K. Liu, Z. Xiang, J. Ying, Z. Wang, T. Wu, and X. Chen, *Charge-density-wave-driven electronic nematicity in a kagome superconductor*, Nature **604**, 59–64 (2022).
- [11] Y. Xu, Z. Ni, Y. Liu, B. R. Ortiz, Q. Deng, S. D. Wilson, B. Yan, L. Balents, and L. Wu, *Three-state nematicity and magneto-optical Kerr effect in the charge density waves in kagome superconductors*, Nat. Phys. **18**, 1470–1475 (2022).
- [12] M. Roppongi, K. Ishihara, Y. Tanaka, K. Ogawa, K. Okada, S. Liu, K. Mukasa, Y. Mizukami, Y. Uwatoko, R. Grasset, M. Konczykowski, B. R. Ortiz, S. D. Wilson, K. Hashimoto, and T. Shibauchi, *Bulk evidence of anisotropic s-wave pairing with no sign change in the kagome superconductor CsV_3Sb_5* , arXiv:2206.02580 (available at <https://arxiv.org/abs/2206.02580>).
- [13] W. Zhang, X. Liu, L. Wang, C. W. Tsang, Z. Wang, S. T. Lam, W. Wang, J. Xie, X. Zhou, Y. Zhao, S. Wang, J. Tallon, K. T. Lai, and S. K. Goh, *Nodeless superconductivity in kagome metal CsV_3Sb_5 with and without time reversal symmetry breaking*, arXiv:2301.07374 (available at <https://arxiv.org/abs/2301.07374>).
- [14] Z. Guguchia, D.J. Gawryluk, Soohyeon Shin, Z. Hao, C. Mielke III, D. Das, I. Plokhikh, L. Liborio, K. Shenton, Y. Hu, V. Szagari, M. Medarde, H. Deng, Y. Cai, C. Chen, Y. Jiang, A. Amato, M. Shi, M.Z. Hasan, J.-X. Yin, R. Khasanov, E. Pomjakushina, and H. Luetkens, *Hidden magnetism uncovered in charge ordered bilayer kagome material ScV_6Sn_6* , arXiv:2304.06436
- [15] X. Wu, T. Schwemmer, T. Müller, A. Consiglio, G. Sangiovanni, D. Di Sante, Y. Iqbal, W. Hanke, A. P. Schnyder, M. M. Denner, M. H. Fischer, T. Neupert, and R. Thomale, *Nature of Unconventional Pairing in the Kagome Superconductors AV_3Sb_5 ($A = \text{K, Rb, Cs}$)*, Phys. Rev. Lett. **127**, 177001 (2021).
- [16] M. M. Denner, R. Thomale, and T. Neupert, *Analysis of Charge Order in the Kagome Metal AV_3Sb_5 ($A = \text{K, Rb, Cs}$)*, Phys. Rev. Lett. **127**, 217601 (2021).
- [17] T. Park, M. Ye, and L. Balents, *Electronic instabilities of kagome metals: Saddle points and Landau theory*, Phys. Rev. B **104**, 035142 (2021).
- [18] R. Tazai, Y. Yamakawa, S. Onari, and H. Kontani, *Mechanism of exotic density-wave and beyond-Migdal unconventional superconductivity in kagome metal AV_3Sb_5 ($A = \text{K, Rb, Cs}$)*, Sci. Adv. **8**, eabl4108 (2022).
- [19] R. Tazai, Y. Yamakawa and H. Kontani, *Charge-loop current order and Z_3 nematicity mediated by bond-order fluctuations in kagome metals*, Nat. Commun. **14**, 7845 (2023).

- [20] R. Tazai, Y. Yamakawa and H. Kontani, *Drastic magnetic-field-induced chiral current order and emergent current-bond-field interplay in kagome metals*, Proceedings of the National Academy of Sciences (PNAS) **121**, e2303476121 (2024).
- [21] M. H. Christensen, T. Biro, B. M. Andersen, and R. M. Fernandes, *Loop currents in AV₃Sb₅ kagome metals: Multipolar and toroidal magnetic orders*, Phys. Rev. B **106**, 144504 (2022).
- [22] F. Grandi, A. Consiglio, M. A. Sentef, R. Thomale, and D. M. Kennes, *Theory of nematic charge orders in kagome metals*, Phys. Rev. B **107**, 155131 (2023).
- [23] H. D. Scammell, J. Ingham, T. Li, and O. P. Sushkov, *Chiral excitonic order from twofold van Hove singularities in kagome metals*, Nat. Commun. **14**, 605 (2023).
- [24] Y. Hu, C. Le, Z. Zhao, J. Ma, N. C. Plumb, M. Radovic, A. P. Schnyder, X. Wu, H. Chen, X. Dong, J. Hu, H. Yang, H.-J. Gao, and M. Shi, *Non-trivial band topology and orbital-selective electronic nematicity in a titanium-based kagome superconductor*, Nat. Phys. **19**, 1827 (2023).
- [25] Z. Rehfuss, C. Broyles, D. Graf, Y. Li, H. Tan, Z. Zhao, J. Liu, Y. Zhang, X. Dong, H. Yang, H. Gao, B. Yan, and S. Ran, *Quantum Oscillations in kagome metals CsTi₃Bi₅ and RbTi₃Bi₅*, arXiv:2401.13628.
- [26] H. Yang, Z. Zhao, X.-W. Yi, J. Liu, J.-Y. You, Y. Zhang, H. Guo, X. Lin, C. Shen, H. Chen, X. Dong, G. Su, and H.-J. Gao, *Titanium-based kagome superconductor CsTi₃Bi₅ and topological states*, arXiv:2209.03840.
- [27] D. Werhahn, B. R. Ortiz, A. K. Hay, S. D. Wilson, R. Seshadri, and D. Johrendt, *The kagome metals RbTi₃Bi₅ and CsTi₃Bi₅*, Z. Naturforsch. **77b**, 757 (2022).
- [28] H. Li, S. Cheng, B. R. Ortiz, H. Tan, D. Werhahn, K. Zeng, D. Jorhndt, B. Yan, Z. Wang, S. D. Wilson, and I. Zeljkovic, *Electronic nematicity in the absence of charge density waves in a new titanium-based kagome metal*, Nat. Phys. **19**, 1591 (2023).
- [29] H. Yang, Y. Ye, Z. Zhao, J. Liu, X.-W. Yi, Y. Zhang, J. Shi, J.-Y. You, Z. Huang, B. Wang, J. Wang, H. Guo, X. Lin, C. Shen, W. Zhou, H. Chen, X. Dong, G. Su, Z. Wang, H.-J. Gao, *Superconductivity and orbital-selective nematic order in a new titanium-based kagome metal CsTi₃Bi₅*, arXiv:2211.12264.
- [30] Y. Wang *et al.*, *Flat Band and Z₂ Topology of Kagome Metal CsTi₃Bi₅*, Chin. Phys. Lett. **40**, 037102 (2023).
- [31] X. Chen, X. Liu, W. Xia, X. Mi, L. Zhong, K. Yang, L. Zhang, Y. Gan, Y. Liu, G. Wang, A. Wang, Y. Chai, J. Shen, X. Yang, Y. Guo, and M. He, *Electrical and thermal transport properties of the kagome metals ATi₃Bi₅ (A=Rb,Cs)*, Phys. Rev. B **107**, 174510 (2023).
- [32] S. Onari and H. Kontani, *Self-consistent Vertex Correction Analysis for Iron-based Superconductors: Mechanism of Coulomb Interaction-Driven Orbital Fluctuations*, Phys. Rev. Lett. **109**, 137001 (2012).
- [33] Y. Yamakawa, S. Onari, and H. Kontani, *Nematicity and Magnetism in FeSe and Other Families of Fe-Based Superconductors*, Phys. Rev. X **6**, 021032 (2016).
- [34] S. Onari and H. Kontani, *SU(4) Valley+Spin Fluctuation Interference Mechanism for Nematic Order in Magic-Angle Twisted Bilayer Graphene: The Impact of Vertex Corrections*, Phys. Rev. Lett. **128**, 066401 (2022).
- [35] M. Tsuchiizu, Y. Ohno, S. Onari, and H. Kontani, *Orbital Nematic Instability in the Two-Orbital Hubbard Model: Renormalization-Group + Constrained RPA Analysis*, Phys. Rev. Lett. **111**, 057003 (2013).
- [36] M. Tsuchiizu, K. Kawaguchi, Y. Yamakawa, and H. Kontani, *Multistage electronic nematic transitions in cuprate superconductors: A functional-renormalization-group analysis*, Phys. Rev. B **97**, 165131 (2018).
- [37] R. Tazai, Y. Yamakawa, M. Tsuchiizu, and H. Kontani, *d- and p-wave Quantum Liquid Crystal Orders in Cuprate Superconductors, κ -(BEDT-TTF)₂X, and Coupled Chain Hubbard Models: Functional-renormalization-group Analysis*, J. Phys. Soc. Jpn. **90**, 111012 (2021).
- [38] A. V. Chubukov, M. Khodas, and R. M. Fernandes, *Magnetism, Superconductivity, and Spontaneous Orbital Order in Iron-Based Superconductors: Which Comes First and Why?*, Phys. Rev. X **6**, 041045 (2016).
- [39] R. M. Fernandes, P. P. Orth, and J. Schmalian, *Intertwined Vestigial Order in Quantum Materials: Nematicity and Beyond*, Annu. Rev. Condens. Matter Phys. **10**, 133 (2019).
- [40] H. Kontani, R. Tazai, Y. Yamakawa, and S. Onari, *Unconventional density waves and superconductivities in Fe-based superconductors and other strongly correlated electron systems*, Adv. Phys. **70**, 355 (2021).
- [41] J. C. S. Davis and D.-H. Lee, *Concepts relating magnetic interactions, intertwined electronic orders, and strongly correlated superconductivity*, Proc. Natl. Acad. Sci. U.S.A. **110**, 17623 (2013).
- [42] K. Mukasa, K. Ishida, S. Imajo, M. Qiu, M. Saito, K. Matsuura, Y. Sugimura, S. Liu, Y. Uezono, T. Otsuka, M. Culo, S. Kasahara, Y. Matsuda, N. E. Hussey, T. Watanabe, K. Kindo, and T. Shibauchi, *Enhanced Superconducting Pairing Strength near a Pure Nematic Quantum Critical Point*, Phys. Rev. X **13**, 011032 (2023).
- [43] Supplementary Materials.
- [44] N. E. Bickers, D. J. Scalapino, S. R. White, Phys. Rev. Lett. **62**, 961 (1989).
- [45] H. Kontani, K. Kanki, and K. Ueda, Phys. Rev. B **59**, 14723 (1999).
- [46] H. Kontani, Rep. Prog. Phys. **71**, 026501 (2008).
- [47] R. Tazai, S. Matsubara, Y. Yamakawa, S. Onari, and H. Kontani, *Rigorous formalism for unconventional symmetry breaking in Fermi liquid theory and its application to nematicity in FeSe*, Phys. Rev. B **107**, 035137 (2023).
- [48] S. Onari and H. Kontani, *Origin of diverse nematic orders in Fe-based superconductors: 45° rotated nematicity in AF₂A₂ (A=Cs,Rb)*, Phys. Rev. B **100**, 020507(R) (2019).
- [49] V. Kozii and L. Fu, *Odd-Parity Superconductivity in the Vicinity of Inversion Symmetry Breaking in Spin-Orbit-Coupled Systems*, Phys. Rev. Lett. **115**, 207002 (2015).
- [50] S. Hayami, Y. Yanagi, H. Kusunose, and Y. Motome, *Electric Toroidal Quadrupoles in the Spin-Orbit-Coupled Metal Cd₂Re₂O₇*, Phys. Rev. Lett. **122**, 147602 (2019).
- [51] H. T. Hirose, T. Terashima, D. Hirai, Y. Matsubayashi, N. Kikugawa, D. Graf, K. Sugii, S. Sugiura, Z. Hiroi, and S. Uji, *Electronic states of metallic electric toroidal quadrupole order in Cd₂Re₂O₇ determined by combining quantum oscillations and electronic structure calculations*, Phys. Rev. B **105**, 035116 (2022).
- [52] J. W. Harter, Z. Y. Zhao, J.-Q. Yan, D. G. Mandrus, and D. Hsieh, *A parity-breaking electronic nematic phase transition in the spin-orbit coupled metal Cd₂Re₂O₇*, Science **356**, 6335 (2017).
- [53] Y.-W. Fang and H. Chen, *Design of a multifunctional polar metal via first-principles high-throughput structure*

- screening*, Communications Materials **1**, 1 (2020).
- [54] M. Yi, H. Pfau, Y. Zhang, Y. He, H. Wu, T. Chen, Z. Ye, M. Hashimoto, R. Yu, Q. Si, D.-H. Lee, P. Dai, Z.-X. Shen, D. Lu, and R. J. Birgeneau, *Nematic Energy Scale and the Missing Electron Pocket in FeSe*, Phys. Rev. X **9**, 041049 (2019).
- [55] I. Sodemann and L. Fu, *Quantum nonlinear Hall effect induced by Berry curvature dipole in time-reversal invariant materials*, Phys. Rev. Lett. **115**, 216806 (2015).
- [56] Q. Ma *et al.*, *Observation of the nonlinear Hall effect under time-reversal-symmetric conditions*, Nature **565**, 337 (2019).
- [57] M. Huang, Z. Wu, X. Zhang, X. Feng, Z. Zhou, S. Wang, Y. Chen, C. Cheng, K. Sun, Z. Y. Meng, and N. Wang, *Intrinsic Nonlinear Hall Effect and Gate-Switchable Berry Curvature Sliding in Twisted Bilayer Graphene*, Phys. Rev. Lett. **131**, 066301 (2023).
- [58] Z. Z. Du, H.-Z. Lu and X. C. Xie, *Nonlinear Hall effects*, Nature Reviews Physics **3**, 744 (2021).
- [59] J. Orenstein, J.E. Moore, T. Morimoto, D.H. Torchinsky, J.W. Harter, and D. Hsieh, *Topology and Symmetry of Quantum Materials via Nonlinear Optical Responses*, Annu. Rev. Cond. Mat. Phys. **12**, 247 (2021).
- [60] Y. Yanase, *Magneto-Electric Effect in Three-Dimensional Coupled Zigzag Chains*, J. Phys. Soc. Jpn. **83**, 014703 (2014).

[Supplementary Materials]

Odd-parity quadrupole order and induced nonreciprocal transport in kagome metal CsTi_3Bi_5 driven by quantum interference mechanism

Jianxin Huang¹, Youichi Yamakawa¹, Rina Tazai², Takahiro Morimoto³, and Hiroshi Kontani¹

¹Department of Physics, Nagoya University, Nagoya 464-8602, Japan

²Yukawa Institute for Theoretical Physics, Kyoto University, Kyoto 606-8502, Japan

³Department of Applied Physics, The University of Tokyo, Tokyo 113-8656, Japan

A: Band calculation for CsTi_3Bi_5

Here, we derive the first-principles realistic tight-binding model for CsTi_3Bi_5 . First, we perform the band calculation based on the WIEN2k software, by using the crystal structure reported in Ref. [1]. The Fermi surfaces are essentially two-dimensional because the inter-layer hopping integrals are small. The large cylindrical FS around Γ point is mainly composed of the xy orbital of Ti $3d$ electrons. The two cylindrical FSs around K, K' points are composed of xz orbital electrons. Thus, the major FSs of CsTi_3Bi_5 are mainly composed of two d -orbitals (xy and xz) of Ti-ions on sublattice A,B,C. The bandstructure with xy -orbital weight and that with xz -orbital weight are shown in Figs. S1 (a) and (b), respectively. Each d -orbital DOS is shown in Fig. S1 (c). Other less-important d orbital weights are shown in Figs. S2 (a)-(c).

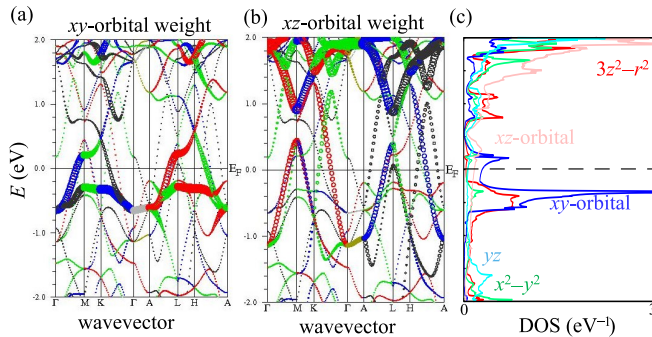


FIG. S1. Bandstructures with (a) xy -orbital weight and (b) xz -orbital weight denoted by the size of each circle. (c) Each d -orbital DOS.

In the obtained bandstructure, the spin-orbit coupling (SOC) is neglected. The effect of the SOC is large for the Bi $6p$ -orbital band that gives the small Fermi pocket around Γ point, while the major $3d$ -orbital bands are affected by the SOC only slightly [1]. Therefore, the effect of the SOC is safely neglected. We just introduce the shift of the xy -orbital level $\delta E_{xy} = -0.15\text{eV}$ to represent the self hole-doping due to the SOC-induced enlargement of $6p$ orbital electron pocket around Γ point.

Next, we derive the 30 orbital tight-binding model by

using Wannier90 software. In the main text, we use the two-dimensional model by neglecting the small inter-layer hopping integrals. Based on the obtained model for CsTi_3Bi_5 , we performed the multiorbital random-phase-approximation (RPA) to find out the significant d -orbitals with strong electron correlations. We revealed that the spin Stoner factor α_S reaches unity when intra-orbital term $U = 1.62$ (RPA), inter-orbital term $U' = U - 2J$, and exchange term $J = 0.1U$ are used for the six-orbital ($3b_{3g} + 3b_{2g}$) Coulomb interaction. When $\alpha_S \gtrsim 0.9$, the spin susceptibility develops only for the xy -orbital; $\chi_{xy}^s(\mathbf{q})$.

It is verified that both α_S and $\chi_{xy}^s(\mathbf{q})$ are almost unchanged even if only the intra xy -orbital Coulomb interaction $U_{xy} = 2.18$ (RPA) is taken into account in the numerical study. (If only intra xz -orbital interaction U_{xz} is considered, large $U = 5.29$ (RPA) is needed for realizing $\alpha_S = 1$.) Therefore, the spin fluctuations in Ti-based kagome metal is highly orbital selective. In the main text, we study the nematic order due to the paramagnon interference mechanism. Since the paramagnon develops only on xy -orbital, we introduce only the xy -orbital Coulomb interaction in the FLEX and DW equation analyses in the main text.

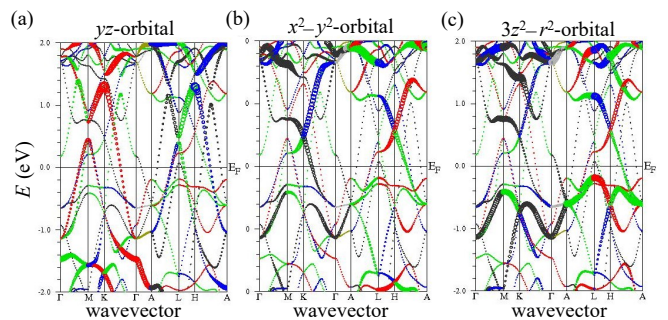


FIG. S2. Bandstructures with (a) yz -orbital weight, (b) $x^2 - y^2$ -orbital weight, and (c) $3z^2 - r^2$ -orbital weight.

B: FLEX self-energy and DW equation

In the main text, we calculate the spin susceptibility by including the self-energy effect self-consistently. For

this purpose, we use the fluctuation-exchange (FLEX) approximation [2–4]:

$$\Sigma_{l,m}(k) = \frac{T}{N} \sum_q G_{l,m}(k-q) V_{l,m}(q), \quad (\text{S1})$$

$$V_{l,m}(q) = \frac{U^2}{2} (3\chi_{l,m}^s(q) + \chi_{l,m}^c(q) - \chi_{l,m}^0(q)), \quad (\text{S2})$$

$$\chi_{l,m}^0(q) = -\frac{T}{N} \sum_k G_{l,m}(k+q) G_{m,l}(k), \quad (\text{S3})$$

$$\hat{\chi}^{s(c)}(q) = \hat{\chi}^0(q) (\hat{1} - (+)U\hat{\chi}^0(q))^{-1} \quad (\text{S4})$$

where the indices l, m represent the xy -orbital at sublattice A, B, C, $k \equiv (\mathbf{k}, \epsilon_n) = (2n+1)\pi T$ and $q \equiv (\mathbf{q}, \omega_l) = 2l\pi T$. $\Sigma_{l,m}(k)$ is the self-energy shown in Fig. S3 (a), $\chi_{l,m}^{s(c)}(q)$ is the spin (charge) susceptibility, and $G_{l,m}(k)$ is the Green function on the xy -orbital. U is the Coulomb interaction on the xy -orbital. Here, $G_{l,m}(k) = ((i\epsilon_n + \mu)\hat{1} - \hat{h}_{\mathbf{k}}^0 - \hat{\Sigma}(k))_{l,m}^{-1}$, where $\hat{h}_{\mathbf{k}}^0$ is 30×30 matrix expression of the kinetic term given by the Fourier transform of the present tight-binding model. (Note that the matrix elements of $\hat{\Sigma}(k)$ is zero except for three xy -orbitals.) Here, we solve Eqs. (S1)-(S4) self-consistently. In the numerical study, we use 60×60 \mathbf{k} -meshes and 8192 Matsubara frequencies.

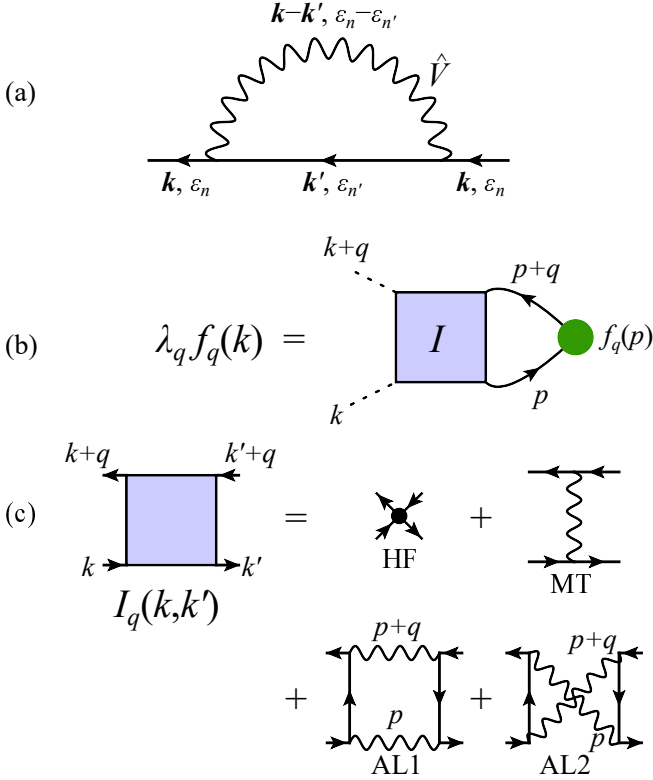


FIG. S3. (a) Diagrammatic expression of the self-energy. (b) Diagrammatic expression of the DW equation. (c) Kernel function I composed of one Hartree term, one MT term, and two AL terms. Note that simple local charge density order are prohibited by the Hartree term.

Figure S3 (b) shows the diagrammatic expression of the DW equation, which is given in Eq. (1) in the main text. The kernel function I given by the Ward identity ($I = \delta\Sigma/\delta G$) is composed of one single-magnon exchange term and two double-magnon interference terms. The former is called the Maki-Thompson (MT) term, and the latter is called the AL terms. Its derivation based on the Luttinger-Ward free-energy theory is given in Ref. [5] and in the SM D. We verified that the AL (MT) contribution to the E_{1u} state is $\lambda_{E_{1u}}^{\text{AL}} = 0.75$ ($\lambda_{E_{1u}}^{\text{MT}} = 0.27$). It is noteworthy that $\lambda_{E_{1u}}^{\text{Hartree}} = 0$.

Here, we explain the essential role of the AL terms for the charge channel density-wave (DW); $\hat{f}^c \equiv (\hat{f}^\uparrow + \hat{f}^\downarrow)/2$. The kernel function for AL1 (I^+) and AL2 (I^-) are approximately given as $I_q^\pm(k, k') \approx T \sum_p \frac{3U^4}{2} G(k \pm p) G(k' - p) X_q(p)$, where $X_q(p) = \chi^s(p) \chi^s(p+q)$. The present interference between two paramagnons gives rise to the charge-channel DW constructively in the DW equation. Importantly, this process does not contribute to the spin-channel DW, $\hat{f}^s \equiv (\hat{f}^\uparrow - \hat{f}^\downarrow)/2$, because the two-paramagnon process preserves the time-reversal symmetry [12]. In FeSe, the AL terms drive the nonmagnetic nematic order. The importance of AL terms was verified by the functional-renormalization-group (fRG) study [12].

Below, we discuss why the AL terms give the E_{1u} BO in Ti-based kagome metal with the sublattice degrees of freedom. The AL terms in Fig. S3 (c) for the form factor $f^{l,m}$ is approximately proportional to the convolution $X_{lm}(\mathbf{q}) = \frac{1}{N} \sum_p \chi_{l,l}^s(\mathbf{p}) \chi_{m,m}^s(\mathbf{p} + \mathbf{q})$ ($l, m = \text{A, B, C}$). In general, the eigenvalue at \mathbf{q} is roughly proportional to $X_{lm}(\mathbf{q})$, which is large when $\mathbf{q} \sim \mathbf{0}$ and the peak (the width) of $\chi^s(\mathbf{p})$ is high (broad). Figure S4 (a) shows $\{\chi_{\text{A,A}}^s(\mathbf{q})\}^2$ and $\chi_{\text{A,A}}^s(\mathbf{q}) \chi_{\text{C,C}}^s(\mathbf{q})$ in the present model at $\alpha_S = 0.9$. Due to the broadness of the peak of $\chi_{\text{A,A}}^s(\mathbf{q})$ shown in Fig. 1 (d), $\frac{1}{N} \sum_q \chi_{\text{A,A}}^s(\mathbf{q}) \chi_{\text{C,C}}^s(\mathbf{q}) = 1.81$ is as large as $\frac{1}{N} \sum_q \{\chi_{\text{A,A}}^s(\mathbf{q})\}^2 = 1.83$. This situation is favorable for the E_{1u} BO given by the inter-sublattice form factor shown in Fig. 3 (a).

The symmetry of the form factor is determined by the momentum-dependence of $I(\mathbf{k}, \mathbf{k}')$. Figure S4 (b) shows the AL1 term $I_{\text{CA,CA}}^{\text{AL1}}(\mathbf{k}_{\text{CA}}, \mathbf{k})$ and AL2 term $I_{\text{CA,AC}}^{\text{AL2}}(\mathbf{k}_{\text{CA}}, \mathbf{k}')$. As we explained in Ref. [6] and Ref. [7], the AL1 term gives the attractive interaction for $\mathbf{k} \approx \mathbf{k}_{\text{CA}}$. In contrast, the AL2 term gives the attractive interaction for $\mathbf{k}' \approx -\mathbf{k}_{\text{CA}}$, as depicted in Fig. S4 (c). Such \mathbf{k} -dependence originates from the particle-hole pair $G(p)G(p)$ in the AL1 term and the particle-particle pair $G(p)G(-p)$ in the AL2 term [6, 7]. Both [AL1] and [AL2] cooperatively contribute to the odd-parity BO, as we explain in the main text.

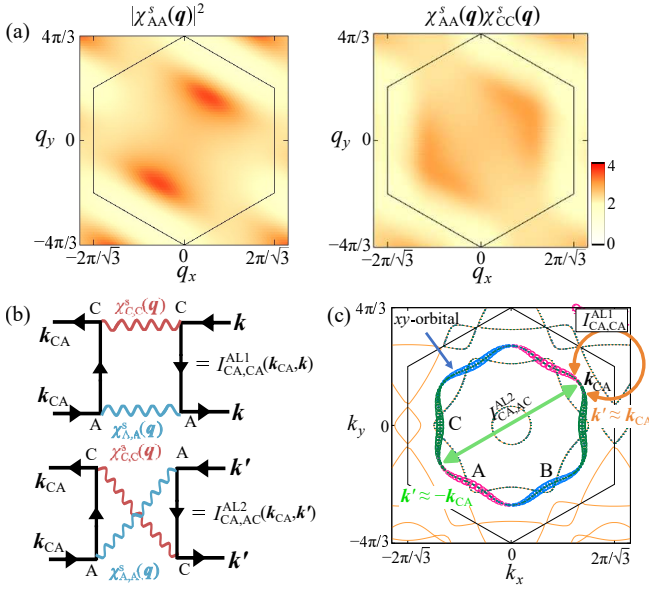


FIG. S4. (a) $X_{A,A}(\mathbf{q}) \equiv \{\chi_{A,A}^s(\mathbf{q})\}^2$ and $X_{A,C}(\mathbf{q}) \equiv \chi_{A,A}^s(\mathbf{q})\chi_{C,C}^s(\mathbf{q})$. (b) AL1 term $I_{CA,CA}^{AL1}(\mathbf{k}_{CA}, \mathbf{k})$ and AL2 term $I_{CA,AC}^{AL2}(\mathbf{k}_{CA}, \mathbf{k}')$. (c) Attraction given by AL1 and AL2 terms. The weights of the sublattices A (red), B (blue), and C (green) are shown.

C: Form factor and symmetry breaking in self-energy

In strongly correlated metals, various kinds of the density-wave (DW) orders emerges, such as the spin/charge density waves, the even/odd parity bond orders, and the charge/spin current orders. These DW orders are represented as the symmetry breaking in the self-energy [5]. Here, we focus on the DW at $\mathbf{q} = \mathbf{0}$. By following Ref. [5], we divide the self-energy into

$$\hat{\Sigma}(k) = \hat{\Sigma}^0(k) + \delta\hat{t}(k), \quad (\text{S5})$$

where $\hat{\Sigma}^0$ is the ‘‘normal state self-energy’’ without any symmetry breaking, and $\delta\hat{t}$ is equal to the DW order parameter introduced in the SM D. Here, Σ^0 belongs to A_{1g} symmetry, while $\delta\hat{t}$ belongs to non- A_{1g} symmetry. Thus, $\delta t = 0$ for $T > T_c$. Hereafter, we denote $\delta\hat{t}(k) \equiv \phi\hat{f}(k)$, where $\hat{f}(k)$ is the form factor that is normalized as $\max_{l,m,k} |f_{lm}(k)| = 1$. The form factor is microscopically obtained by solving the DW equation. Another equivalent interpreted of the form factor $f_q^L(k)$ is the particle-hole (p-h) condensation $\sum_{\sigma} \{\langle c_{\mathbf{k}+\mathbf{q},l,\sigma}^{\dagger} c_{\mathbf{k},l',\sigma} \rangle - \langle \cdots \rangle\}$ [5].

Because we consider the thermal equilibrium state, the form factor satisfies the Hermitian condition; $f_q^{l,l'}(k) = (f_{-q}^{l',l}(k+\mathbf{q}))^*$. Here, l and l' is the orbital or the sublattice, and \mathbf{q} is the wavevector of the DW. This condition is directly derived from the Hermitian condition for the hopping integral between sites i and j ; $\delta t_{i,j}^{l,l'} = (\delta t_{j,i}^{l',l})^*$. In the BO without the TRS breaking, $\delta t_{i,j}^{l,l'} = \delta t_{j,i}^{l',l} = \text{real}$.

In the case of E_{1u} BO, the form factor (\hat{f}, \hat{f}') satisfies the relation $f_{AC}(-\mathbf{k}_{CA}) = -\{f_{CA}(\mathbf{k}_{CA})\}^* = f_{CA}(\mathbf{k}_{CA})$. For any form factor \hat{f} , $x\hat{f}$ violates the Hermite condition if x is not real. Therefore, the linear combination of the form factor is always given as $\hat{f}_{\theta} = \hat{f} \cos \theta + \hat{f}' \sin \theta$. This fact is very different from the superconducting state in a 2D irrep (Δ, Δ') , where the chiral state $(\Delta + i\Delta')$ without time-reversal-symmetry is allowed.

In the DW state, the BO without the TRS occurs when $\delta t_{i,j}^{l,l'} = -\delta t_{j,i}^{l',l}$ is imaginary. This charge current order is actively discussed in V-based kagome metals [8].

D: Derivation of DW equation based on Luttinger-Ward free energy theory

The Luttinger-Ward (LW) theory [9] provides an exact expression of the grand potential Ω , which is applicable for strongly correlated metals unless the perturbation treatment is violated. The grand potential is expressed as

$$\Omega = \Omega_F + \Phi, \quad (\text{S6})$$

$$\Omega_F = \frac{T}{N} \sum_{k\sigma} \{ \ln(G_{k\sigma}) - G_{k\sigma} ((G_{k\sigma}^{\text{free}})^{-1} - G_{k\sigma}^{-1}) \}, \quad (\text{S7})$$

$$\Phi = \frac{T}{N} \sum_q \text{Tr} \left\{ \frac{3}{2} \ln(1 - U\chi_q^0) + \frac{1}{2} \ln(1 + U\chi_q^0) \right\} + \frac{T}{N} \sum_q \text{Tr} \left\{ \frac{1}{2} (U\chi_q^0)^2 + U\chi_q^0 \right\}, \quad (\text{S8})$$

where $\frac{T}{N} \sum_k \cdots \equiv \frac{T}{N} \sum_{\epsilon_n} \sum_{\mathbf{k}} \cdots$, and $G_{k\sigma}$ is the Green function with the self-energy: $G_{k\sigma} = ((G_{k\sigma}^{\text{free}})^{-1} - \Sigma_{k\sigma})^{-1}$. Here, Φ is the Luttinger-Ward function, which satisfies the relation $\delta\Phi/\delta G_k = \Sigma_k$. Φ in the FLEX scheme is given in Fig. S5 (a) and in Eq. (S8), which gives a negative logarithmic divergence for $\alpha_S \rightarrow 1$. This term represents the gain in the free energy due to the spin (bosonic) fluctuations.

The thermal equilibrium state is given by the stationary point of the ground potential; $\delta\Omega/\delta\Sigma_{k\sigma} = 0$ [9]. Here, we derive the DW equation from the following stationary conditions by following Ref. [5]:

$$\left. \frac{\delta\Omega}{\delta\Sigma_{k\sigma}} \right|_{\Sigma^0} = 0, \quad (\text{at any } T) \quad (\text{S9})$$

$$\left. \frac{\delta\Omega}{\delta\Sigma_{k\sigma}} \right|_{\bar{\Sigma}} = 0 \quad (T < T_c), \quad (\text{S10})$$

where Σ^0 is the self-energy without any symmetry breaking, and $\bar{\Sigma}$ is the stationary self-energy after the symmetry breaking. For $T > T_c$, the thermodynamic state is given by Eq. (S9), which corresponds to the minimum of the free energy shown in Fig. S5 (b). For $T < T_c$, Eq. (S10) gives the symmetry breaking state shown in

Fig. S5 (c). (Eq. (S10) corresponds to the unstable extremum.)

Based on Eq.(S7), we obtain

$$\begin{aligned} \frac{\delta\Omega}{\delta\Sigma_{k\sigma}} &= -G_{k\sigma}^2 \Sigma_{k\sigma} + \frac{\delta\Phi}{\delta\Sigma_{k\sigma}} \\ &= -G_{k\sigma}^2 \Sigma_{k\sigma} + \frac{T}{N} \sum_{k'\sigma'} \frac{\delta G_{k'\sigma'}}{\delta\Sigma_{k\sigma}} \frac{\delta\Phi}{\delta G_{k'\sigma'}}, \end{aligned} \quad (\text{S11})$$

where $\frac{\delta G_{k'\sigma'}}{\delta\Sigma_{k\sigma}} = G_{k\sigma}^2 \delta_{kk'}$. Thus, the stationary condition given by Eqs. (S9) or (S10) is rewritten as

$$\left. \frac{\delta\Phi}{\delta G_{k\sigma}} \right|_{G^0} = \Sigma_{k\sigma}^0, \quad (\text{S12})$$

$$\left. \frac{\delta\Phi}{\delta G_{k\sigma}} \right|_{\bar{G}} = \bar{\Sigma}_{k\sigma}, \quad (\text{S13})$$

where $\hat{G}^0 = (\{\hat{G}^{\text{free}}\}^{-1} - \hat{\Sigma}^0)^{-1}$. Equations (S12) and (S13) compose the ‘‘exact DW equation’’ that describes the DW state below T_c . Then, the order parameter is $\delta t_{k\sigma} = \bar{\Sigma}_{k\sigma} - \Sigma_{k\sigma}^0$.

Next, we derive the ‘‘linearized DW equation’’ with respect to δt by following Ref. [5]. By subtracting Eq. (S12) from (S13), we obtain

$$\begin{aligned} \delta t_{k\sigma} &= \frac{T}{N} \sum_{k'\sigma'} \left. I_{kk'}^{\sigma\sigma'} \right|_{\bar{G}} \delta G_{k'\sigma'} \\ &= \frac{T}{N} \sum_{k'\sigma'} \left. I_{kk'}^{\sigma\sigma'} \right|_{G^0} \delta G_{k'\sigma'} + O(\delta G^2), \end{aligned} \quad (\text{S14})$$

where $\delta G \equiv \bar{G} - G^0$ and $I_{kk'}^{\sigma\sigma'} \equiv \partial^2\Phi/\delta G_{k'\sigma'}\delta G_{k\sigma}$ is the irreducible four-point vertex. Here, we rewrite $\delta t_{k\sigma}$ as

$$\delta t_{k\sigma} \equiv \phi \cdot f_{k\sigma}, \quad (\text{S15})$$

where ϕ is a real parameter, and f_k^q is the normalized order parameter that belongs to one of the irreducible representations in non- A_{1g} symmetry. It is convenient to set $\max_k |f_{k\sigma}| = 1$ because the relation $\phi = \max_k |\delta t_{k\sigma}|$ holds. Thus, we derive the following ‘‘linearize DW equation for $\mathbf{q} = \mathbf{0}$ ’’ by introducing the eigenvalue λ to the left-hand side of Eq. (S14);

$$\lambda f_{k\sigma} = \frac{T}{N} \sum_{k'\sigma'} \left. I_{kk'}^{\sigma\sigma'} \right|_{\Sigma^0} (G_{k'\sigma'}^0)^2 f_{k'\sigma'}, \quad (\text{S16})$$

where we denote $I_{kk'}^{\sigma\sigma'} \equiv \left. I_{kk'}^{\sigma\sigma'} \right|_{\Sigma^0}$ to simplify the notation. Its diagrammatic expression in the FLEX scheme is given in Fig. S4 (c). In Eq. (S16), the largest eigenvalue λ reaches unity at $T = T_c$, and its eigenvector gives the form factor of the DW state. In Ref. [5], the authors discussed the Ginzburg-Landau (GL) free energy based on the Luttinger-Ward-Potthoff theory. The \mathbf{q} -dependent second-order GL coefficient is simply given by the form factor and the eigenvalue derived from the DW equation (S16).

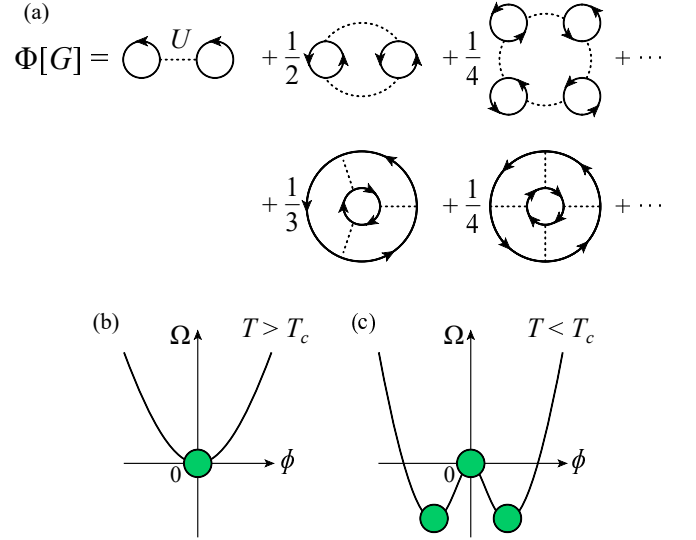


FIG. S5. (a) Diagrammatic expression of Φ in the FLEX scheme. For simplicity, diagrams in the single-orbital Hubbard models are shown, while we study multi-orbital Hubbard models in this paper. (b)(c) Schematic picture of the GL free energy (b) above T_c ($a(T) > 0$) and (c) below T_c ($a(T) < 0$). Stationary points are shown by blue circles. (d) Irreducible vertex I in the FLEX scheme, which is composed of the Hartree-Fock (mean-field) term, the Maki-Thompson (MT) term, and the Aslamazov-Larkin (AL) terms.

Next, we derive the ‘‘full DW equation’’ in the FLEX scheme by following Ref. [5]. The total self-energy is given in Eq. (S5), where Σ^0 is the normal self-energy without any symmetry breaking given by Eq. (S1). (Here, we calculate Σ^0 at each T by subtracting its static and Hermitian part, $\Sigma^{0,H}(\mathbf{k}) \equiv (\Sigma^0(\mathbf{k}, +i\delta) + \Sigma^0(\mathbf{k}, -i\delta))/2$, in order to fix the shape of the FS.) Next, we derive the symmetry breaking part δt self-consistently based on the following procedure: (a) We first calculate $S_k \equiv \frac{T}{N} \sum_q G_{k+q}[\Sigma] V_q[\Sigma]$, where $G_k[\Sigma]$ and $V_q[\Sigma]$ are functions of the total self-energy. (b) Next, we derive δt as

$$\delta t_k = (1 - P_0) S_k, \quad (\text{S17})$$

where P_0 is the projection operator for the totally-symmetric (A_{1g}) channel. (c) The total self-energy is given as $\Sigma = \Sigma_0 + \delta t$. We repeat (a)-(c) till δt converges. It is easy to show that the full-DW equation is equivalent to the linearized-DW equation when δt is very small.

In Ref. [5], the authors performed the full DW equation analysis for FeSe, which is a typical Fe-based superconductors. The electronic nematic order without magnetization and its typical size in FeSe ($\phi \sim 50\text{meV}$ at $T \sim 0$) are satisfactorily obtained.

From now on, we perform the full DW equation analysis for Ti-based kagome metal. In the numerical study, we assume that $\delta t(\mathbf{k})$ is given as $\phi f(\mathbf{k})$, where $f(\mathbf{k})$

is the E_{1u} BO form factor given by the DW equation and ϕ is a constant. This assumption is well satisfied for the nematic order in Fe-based superconductor FeSe [5]. Under this simplification, we have only to obtain the constant ϕ self-consistently numerically. Figure S6 (a) represents the obtained E_{1u} BO parameter ϕ . (Here, $z \equiv (1 - \partial \Sigma_{\mathbf{k}}(\epsilon)/\partial \epsilon|_{\epsilon=0})^{-1} \approx 0.25$ on the FS.) Importantly, the second-order transition occurs at $T_0 \approx 13\text{meV}$, which is consistent with the linearized DW equation analysis in Fig. 2 (d). In Fig. S6 (a), $\phi \sim 0.2$ for $U = 4$ at $T \ll T_0$. The obtained ratio $z\phi/T_0 \approx 4$. This is larger than the BCS ratio (~ 2) because $\mathbf{q} = \mathbf{0}$ BO does not cause the gap in the DOS so the negative feedback is small [5].

Thus, we can set $\phi \sim 0.2$ in analyzing the nematic quasi-particle interference (QPI) signal in CsTi₃Bi₅ ($T_0 \sim 100\text{K}$) in the SM G. (The renormalized order parameter observed by ARPES is $\phi^* \equiv z\phi$, while the band-dispersion is also renormalized by z . Therefore, ϕ should be used to analyze the Fermi surface deformation based on the original (bare) band structure.)

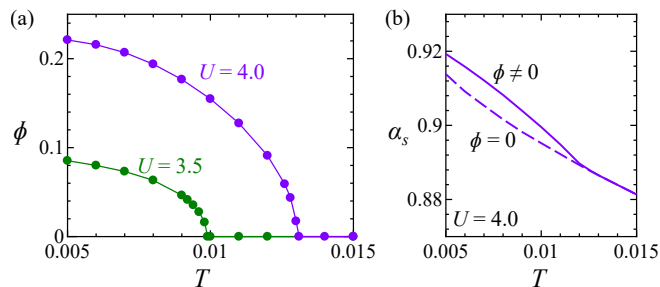


FIG. S6. (a) Obtained E_{1u} -symmetry BO ϕ derived from the full DW equation at $U = 4$. The second-order transition occurs at $T_0 \approx 13\text{meV}$, which is consistent with the linearized DW equation analysis in Fig. 2 (d). (b) Obtained spin Stoner factor α_S when $\phi = 0$ and $\phi \neq 0$ (E_{1u} BO) derived from $\hat{G}^\phi(\mathbf{k})$. The obtained α_S increases in the E_{1u} -symmetry BO state. This result indicates the free-energy gain due to the E_{1u} BO because the LW function Φ is reduced as $\alpha_S \rightarrow 1$. (Note that Φ represents the reduction of the free energy due to the bosonic fluctuations.)

E: Nematic FS deformation by E_{1u} BO for $\theta \neq 0$

We discuss that the present E_{1u} form factor $\hat{f}_\theta \equiv \hat{f} \cos \theta + \hat{f}' \sin \theta$ gives the nematic FS deformation. Here, we introduce the symmetry breaking in the self-energy as $\delta i_{\mathbf{k}}^\theta = \phi \hat{f}_\theta(\mathbf{k})$. The FSs are derived from the eigenvalues of $\hat{h}_{\mathbf{k}}^0 + \delta i_{\mathbf{k}}^\theta$. Because \hat{f}_θ belongs to E_{1u} representation, the FS deformation is very small since it is proportional

to ϕ^2 . For this reason, here we set $\phi \sim 1$ to exaggerate the deformation. Figure S7 is the obtained FSs for $\theta = 0, \pi/6, \pi/3, \pi/2, 2\pi/3, 5\pi/6$. We stress that the FS for θ is equal to the FS for $\theta + \pi$ because the FS deformation due to the E_{1u} BO is proportional to ϕ^2 . For this reason, the induced lattice deformation and the kink in the resistivity at T_0 would be quite small, consistently with experimental reports.

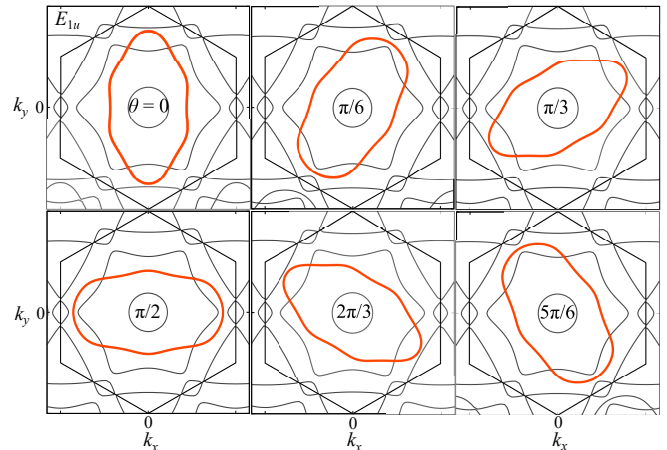


FIG. S7. Nematic FSs at $\theta = 0, \pi/6, \dots, 5\pi/6$ in the E_{1u} BO state at $\phi = 1$.

F: Even-parity E_{2g} BO state at $\mathbf{q} = \mathbf{0}$

In the present DW equation analysis, the $\mathbf{q} = \mathbf{0}$ E_{1u} BO solution is obtained as the largest eigenvalue. Figure S8 shows the first to fourth eigenvalues for $U = 4$ as functions of \mathbf{q} . The first and the second largest eigenvalues correspond to the E_{1u} BOs, and the third and the fourth ones correspond to the E_{2g} BOs. The obtained eigenvalue at $\mathbf{q} = \mathbf{0}$ is 1.11 (0.59) for the E_{1u} (E_{2g}) BO solution at $U = 4$ and $T = 0.01$. Thus, the obtained $\lambda_{E_{2g}}$ is about 0.5 smaller than $\lambda_{E_{1u}}$, because its form factor $g^{C,A}(\mathbf{k}) \propto \cos \mathbf{k} \cdot \mathbf{a}_{CA}$ is smaller than the E_{1u} form factor $f^{C,A}(\mathbf{k})$ in magnitude at $\mathbf{k} \sim \mathbf{k}_{CA}$; see Fig. 3 (a). However, both E_{1u} BO and E_{2g} BO may appear by modifying the model parameters.

The E_{2g} BO solution is doubly degenerate, so its form factor is given by the linear combination of two orthogonal functions $\hat{g}_{\mathbf{k}}$ and $\hat{g}'_{\mathbf{k}}$; that is, $\hat{g}_\theta \equiv \hat{g} \cos \theta + \hat{g}' \sin \theta$. Figure S9 (a) shows the obtained $\hat{g}_{\mathbf{k}}$ for the E_{2g} BO. The realized nematic FS deformation is shown in S9 (b). In the E_{2g} BO, the director of the nematic FS is parallel to $(\cos(\theta + \pi)/2, \sin(\theta + \pi)/2)$. (Note that the director is parallel to $(\cos \theta, \sin \theta)$ in the E_{1u} BO.)

The E_{2g} BO form factor in real space is shown in Figs. S9 (c) and (d). The each E_{2g} BO form factor is invariant under the inversion operation. Thus, the fluctuations of the ferro- E_{2g} BO can be measured as the development

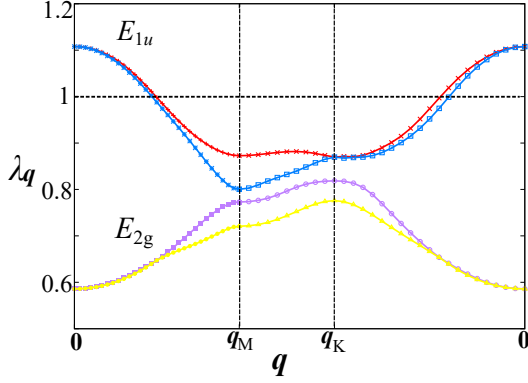


FIG. S8. First to fourth eigenvalues for $U = 4$ as functions of \mathbf{q} . The first and the second largest eigenvalues correspond to the E_{1u} BOs, and the third and the fourth ones correspond to the E_{2g} BOs.

of the nematic susceptibility. In contrast, the ferro- E_{1u} BO fluctuations cannot be observed by the nematic susceptibility measurement because it does not form the bilinear coupling with any share modulus. In fact, the E_{1u} BO form factors shown in Figs. 3 (b) and (c) change their sign under the inversion operation, called the electric toroidal quadrupole order.

G: Δk_F , Δv_F , and anisotropic QPI signal due to odd/even parity BO

First, we analyze the anisotropy of many-body electronic states under the E_{1u} BO. The deformation of the FS and that of the band dispersion are shown in Figs. S10 (a) and (b), respectively. As shown in Fig. S10 (b), large band splitting appears around ②, while the band shift around the Fermi level ① is relatively small. The maximum change in the Fermi momentum $\Delta k_F/G$ and that in the Fermi velocity Δv_F are shown in Figs. S10 (c) and (d), respectively. They are proportional to ϕ^2 in the E_{1u} BO, and the \mathbf{k} points are shown in Fig. S10 (a). Here, $G = 4\pi/\sqrt{3}$ is the reciprocal lattice constant and the averaged Fermi velocity is $v_F \sim 0.5$. Therefore, the relation $|\Delta k_F/G| \ll |\Delta v_F/v_F|$ holds.

In the E_{1u} BO state, the elastic scattering also becomes anisotropic. The impurity scattering strength with the wavevector \mathbf{q} at energy E is $n_{\text{imp}} \text{Im} \sum_{\mathbf{k}, l} \hat{G}^\phi(\mathbf{k}, E) \hat{T}_l \hat{G}^\phi(\mathbf{k} + \mathbf{q}, E)$, where n_{imp} is the impurity concentration and \hat{T}_l is the T -matrix due to a single impurity at sublattice l . Here, we consider the Ti-site unitary impurity potential represented as $(\hat{T}_l)_{m, m'} \sim (-i/\pi N(0)) \delta_{l, m} \delta_{m, m'}$. Then, the impurity scattering strength is approximately proportional to the joint-DOS (JDOS):

$$I^\phi(\mathbf{q}, E) = \sum_{\mathbf{k}, l, m} \rho_{l, m}^\phi(\mathbf{k}, E) \rho_{m, l}^\phi(\mathbf{k} + \mathbf{q}, E), \quad (\text{S18})$$

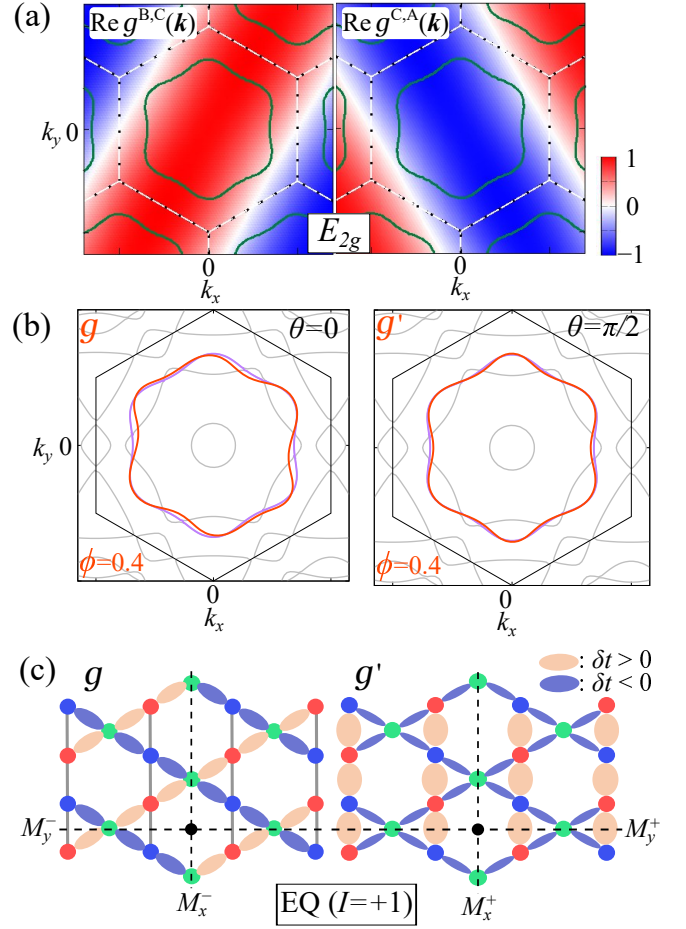


FIG. S9. (a) Form factor of even-parity E_{2g} BO, which corresponds to the second largest eigenvalue at $\mathbf{q} = \mathbf{0}$. (b) Nematic FSs in the E_{2g} BO (\hat{g}, \hat{g}') at $\theta = 0$ and $\pi/2$ for $\phi = 0.4$. (c, d) Even-parity E_{2g} BO form factor (c) \hat{g} and (d) \hat{g}' . They are apparently different from the odd-parity E_{1u} BO \hat{f} and \hat{f}' in Fig. 3 in the main text.

where $\rho_{l, m}^\phi(\mathbf{k}, E) = [G_{l, m}^\phi(\mathbf{k}, E + i0_-) - G_{l, m}^\phi(\mathbf{k}, E - i0_+)]/(2i)$ is the quasiparticle (QP) spectrum. Figure S10 (e) represents the zero-energy JDOS for $\phi = 0$ (=without BO) only for the xy -orbital FSs, $I^{\phi=0}(\mathbf{q}, 0)$. The JDOS corresponds to the QPI signal by STM measurements. The vector \mathbf{q}_i is given by the difference between two Fermi points $\mathbf{k} \approx \mathbf{k}_i$ and $\mathbf{k}' \approx -\mathbf{k}_i$. (Thus, $\mathbf{q}_i \approx 2\mathbf{k}_i$, and \mathbf{k}_i is given in Fig. 1 (c).) For finite ϕ , the JDOS becomes anisotropic. Figure S10 (f) shows the obtained ratios $R_{1-2} = (I_1^\phi - I_2^\phi)/(I_1^\phi + I_2^\phi)$ and $R'_{3-4} = (I_3^\phi - I_4^\phi)/(I_3^\phi + I_4^\phi)$, where $I_i \equiv I^\phi(\mathbf{q}_i, 0)$. Here, we obtain I_m^ϕ ($m = 1 - 4$) as the maximum value of $I^\phi(\mathbf{q}, 0)$ around $\mathbf{q} = \mathbf{q}_i$ because its peak position slightly shifts by $\phi \neq 0$. Because R_{1-2} and R'_{3-4} are negative, the QPI signal is smaller (larger) at $\mathbf{q} = \mathbf{q}_1, \mathbf{q}_3$ ($\mathbf{q} = \mathbf{q}_2, \mathbf{q}_4$). (Note that $R_{2-1} = -R_{1-2}$ and $R'_{3-4} = -R'_{4-3}$.) $R_{1-2} = -0.3$ (-0.5) corresponds to $I_1/I_2 = 0.54$ (0.33). Therefore, the QPI signal exhibit sizable nematic anisotropy in

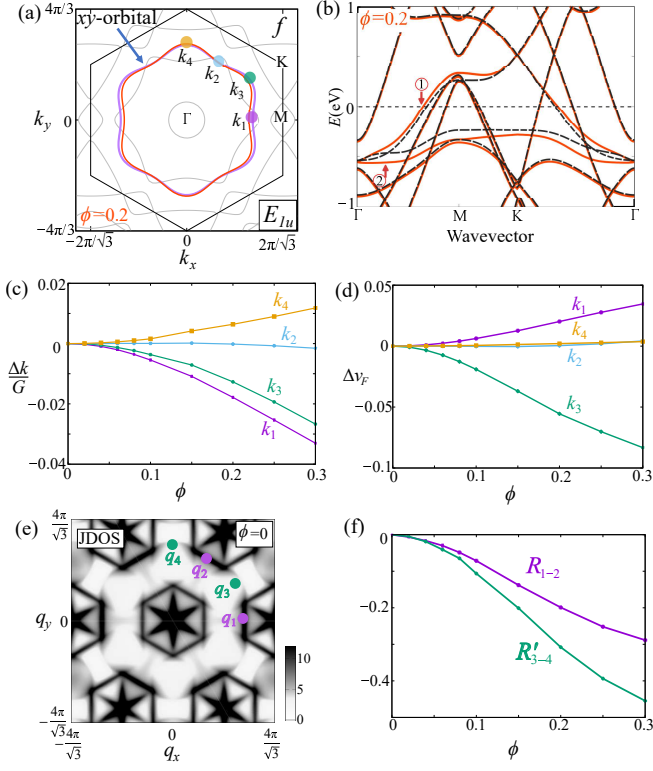


FIG. S10. (a) FS deformation and due to the E_{1u} -symmetry self-energy $\delta\hat{t}_{\mathbf{k}}^{\theta=0} = \phi\hat{f}_{\theta=0}(\mathbf{k})$ for $\phi = 0$ and 0.2. (b) Band dispersion deformation at $\phi = 0$ and 0.2. (c) Deviation of the Fermi momentum $\Delta k_F/G$, where $G = 4\pi/\sqrt{3}$. (d) Deviation of the Fermi velocity Δv_F . (e) QPI signal given by the JDOS approximation for for $\phi = 0$. (f) Anisotropy of the QPI intensity $R_{1-2} \equiv (I_1^\phi - I_2^\phi)/(I_1^\phi + I_2^\phi)$ and $R'_{3-4} \equiv (I_3^\phi - I_4^\phi)/(I_3^\phi + I_4^\phi)$ as function of ϕ . Because R_{1-2} and R'_{3-4} are negative, the QPI signal is smaller (larger) at $\mathbf{q} = \mathbf{q}_1, \mathbf{q}_3$ ($\mathbf{q} = \mathbf{q}_2, \mathbf{q}_4$). (Note that $R_{2-1} = -R_{1-2}$ and $R'_{4-3} = -R'_{3-4}$.) Thus, the QPI signal due to the E_{1u} BO exhibit sizable nematic anisotropy that is comparable to experimental results.

the E_{1u} OB state for $\phi \sim 0.2$, consistently with the experimental results.

Next, we analyze the E_{2g} BO state. The deformations of the FS and the band dispersion, $\Delta k_F/G$, Δv_F are shown in Figs. S11 (a)-(d), respectively. They are proportional to ϕ in the E_{2g} BO. Figure S11 (e) is the anisotropy of the QPI signal due to the E_{2g} BO state, $R_{1-2} = (I_1^\phi - I_2^\phi)/(I_1^\phi + I_2^\phi)$ and $R'_{3-4} = (I_3^\phi - I_4^\phi)/(I_3^\phi + I_4^\phi)$, where $I_i \equiv I^\phi(\mathbf{q}_i, 0)$. $R_{1-2} = 0.1$ corresponds to $I_1/I_2 = 0.82$. The obtained nematic anisotropy by the E_{2g} BO is smaller than that by the E_{1u} BO shown in Fig. S11 (f).

Figure S12 shows the \mathbf{q} -dependence of the QPI signal due to the intra- xy orbital FS scattering, in the cases of (a) without BO ($\phi = 0$), (b) E_{1u} BO ($\phi = 0.3$), and (c) E_{2g} BO ($\phi = 0.3$). In the case of (b) the E_{1u} BO, the QPI signal becomes drastically anisotropic, and the signal is strongly enlarged at $\mathbf{q} = \mathbf{q}_4$. This result is con-

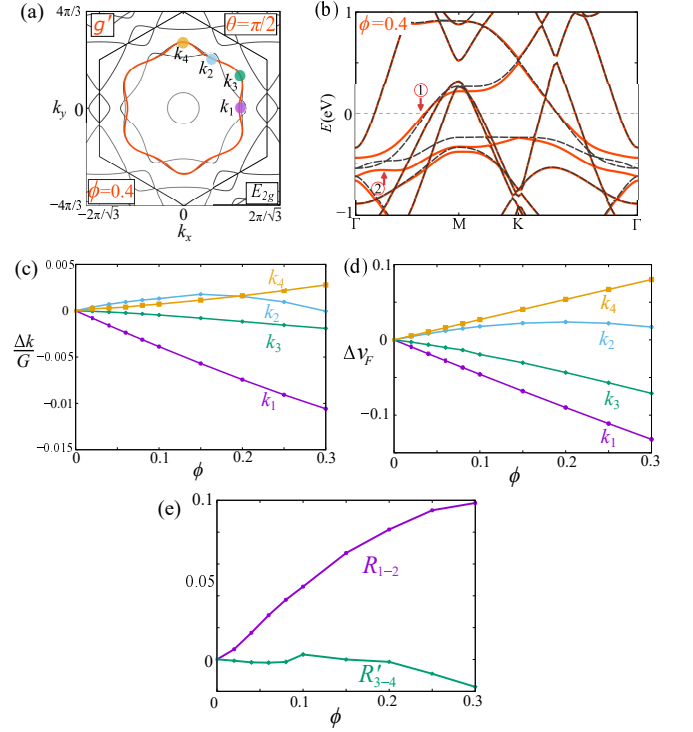


FIG. S11. (a) FS deformation due to the E_{2g} -symmetry self-energy $\delta\hat{t}_{\mathbf{k}}^\theta = \phi\hat{g}_\theta(\mathbf{k})$ for $\phi = 0.4$ at $\theta = \pi/2$. (b) Band dispersion deformation at $\phi = 0.4$. (c) Deformation of the Fermi momentum $\Delta k_F/G$, where $G = 4\pi/\sqrt{3}$. (d) Deformation of the Fermi velocity Δv_F . (e) Anisotropy of the QPI intensity $R_{1-2} \equiv (I_1^\phi - I_2^\phi)/(I_1^\phi + I_2^\phi)$ and $R'_{3-4} \equiv (I_3^\phi - I_4^\phi)/(I_3^\phi + I_4^\phi)$ as function of ϕ . The obtained nematic anisotropy by E_{2g} BO is smaller than experimental result.

sistent with the reports of the STM measurements in Refs. [10, 11]. Note that $|\mathbf{q}_4|$ in this paper corresponds to $|\mathbf{q}_3|$ (\mathbf{q}_4) in Refs. [10] ([11]). In the case of (b) the E_{2g} BO, in contrast, the anisotropy of the QPI signal is almost isotropic, which is inconsistent with experimental reports [10, 11]. Thus, it is concluded that the nematicity in CsTi_3Bi_5 originates from the ETQ BO with E_{1u} symmetry.

We verified that the large QPI anisotropy in the E_{1u} state originates from the inter-sublattice component of the QP spectrum $\rho_{l,m}^\phi(\mathbf{k}, E)$ with $l \neq m$ in the JDOS in Eq. (S18). The anisotropy of the QPI signal due to the inter-sublattice scattering, $\Delta I_{\text{inter}}^\phi(\mathbf{q}_i) \equiv I_{\text{inter}}^\phi(\mathbf{q}_i) - I_{\text{inter}}^{\phi=0}(\mathbf{q}_i)$, is proportional to $\Delta G_{l,m}^\phi(\mathbf{k}_i)\Delta G_{m,l}^\phi(-\mathbf{k}_i)$, where $\Delta G_{l,m}^\phi(\mathbf{k}) \equiv G_{l,m}^\phi(\mathbf{k}) - G_{l,m}^0(\mathbf{k}) \sim \phi G_{l,l}^0(\mathbf{k})f^{l,m}(\mathbf{k})G_{m,m}^0(\mathbf{k})$. Therefore, in the case of the E_{1u} BO, $\Delta I_{\text{inter}}^\phi(\mathbf{q}_i) \sim \phi^2 f^{l,m}(\mathbf{k}_i)f^{m,l}(-\mathbf{k}_i) = -\phi^2 |f^{m,l}(\mathbf{k}_i)|^2$. In the case of the E_{2g} BO, $\Delta I_{\text{inter}}^\phi(\mathbf{q}_i) \sim \phi^2 g^{l,m}(\mathbf{k}_i)g^{m,l}(-\mathbf{k}_i) = \phi^2 |g^{m,l}(\mathbf{k}_i)|^2$. The different sign of $\Delta I_{\text{inter}}^\phi$ between odd-parity and even-parity states gives rise to a qualitative difference in the QPI anisotropy.

Finally, we discuss why the FS deformation (Δk_F) due

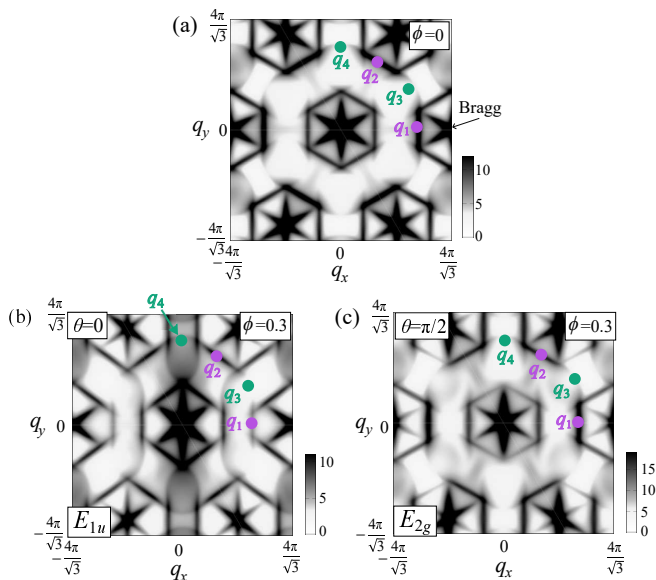


FIG. S12. (a) QPI signal at $\phi = 0$. (b) QPI signal in the E_{1u} BO state and (c) that in the E_{2g} BO state at $\phi = 0.3$.

to the E_{1u} order (ϕ) is proportional to ϕ^2 based on the GL free energy theory. From the symmetry argument, the 3rd order GL free energy with respect to the E_{1u} order $\phi(\cos\theta, \sin\theta)$ and the E_{2g} order $\eta(\cos\theta', \sin\theta')$ is given as $F' = -c\phi^2\eta\cos(2\theta - \theta')$, where c is the GL coefficient. Thus, for a fixed ϕ , the total GL free energy for η up to the 4th order is $F = a\eta^2 + \frac{b}{2}\eta^4 - (c\phi^2)\eta$ when $2\theta = \theta'$. When $a > 0$ (i.e., $T > T_0^{E_{2g}}$), the secondary (or passive) E_{2g} order is obtained as $\eta = (c\phi^2)/a$. Because Δk_F is proportional to the E_{2g} order parameter, we find $\Delta k_F \propto \eta \propto \phi^2$ ($\propto T_0^{E_{1u}} - T$) when $T < T_0^{E_{1u}}$.

To summarize, the E_{1u} BO gives the prominent nematicity observed in CsTi_3Bi_5 [10, 11]. The realized QPI signal anisotropy and the FS deformation Δk_F for $\phi \sim 0.2$ are comparable to experimental report [10, 11]. (Experimentally, $\Delta k_F/G \sim 0.01$, where $G = 4\pi/\sqrt{3}$ is the reciprocal lattice constant [10].) It is noteworthy that the $\phi \sim 0.2$ is obtained by the full DW equation analysis performed in the SM D. Importantly, $\Delta k_F \propto \phi^2$ in the odd-parity BO state, while $\Delta k_F \propto \phi$ in the even-parity BO state. This difference will be useful to determine the symmetry of the BO state. We stress that the finite non-linear Hall (NLH) effect is a crucial evidence for the odd-parity BO. This is an important future issue in Ti-based kagome metals.

H: Relation to 2×2 BO in V-based kagome metals

We briefly discuss the relation between the present E_{1u} BO and 3QBO in AV_3Sb_5 . The quantum interference

mechanism gives rise to the nearest site BO in both Ti-based kagome metal (xy -orbital model) and V-based one (xz -orbital model), while their wavevectors are different. In the latter, since each vHS points consists of one sublattice (=sublattice interference), the nearest site BO is given by the inter-vHS process with finite wavevector. In contrast, in the former, $\mathbf{k} \approx \mathbf{k}_{\text{CA}}$ consisting of C and A sublattices is important for the C-A site BO at $\mathbf{q} = \mathbf{0}$. Thus, the difference in the BO wavevector is naturally understood. The E_{1u} form factor $f^{l,m}(\mathbf{k})$ given in Fig. 3 (a) [$(l, m) = (B, C), (C, A)$] is similar to the form factor of V-based kagome metal, $g_{\mathbf{q}_i}^{l,m}(\mathbf{k} - \mathbf{q}_i/2)$, where \mathbf{q}_i is the CDW wavevector [18]. Both BOs are caused by the paramagnon interference mechanism.

- [1] D. Werhahn, B. R. Ortiz, A. K. Hay, S. D. Wilson, R. Seshadri, and D. Johrendt, *The kagome metals RbTi_3Bi_5 and CsTi_3Bi_5* , *Z. Naturforsch.* **77b**, 757 (2022).
- [2] N. E. Bickers, D. J. Scalapino, S. R. White, *Phys. Rev. Lett.* **62**, 961 (1989).
- [3] H. Kontani, K. Kanki, and K. Ueda, *Phys. Rev. B* **59**, 14723 (1999).
- [4] H. Kontani, *Rep. Prog. Phys.* **71**, 026501 (2008).
- [5] R. Tazai, S. Matsubara, Y. Yamakawa, S. Onari, and H. Kontani, *Rigorous formalism for unconventional symmetry breaking in Fermi liquid theory and its application to nematicity in FeSe* , *Phys. Rev. B* **107**, 035137 (2023).
- [6] H. Kontani, Y. Yamakawa, R. Tazai, and S. Onari, *Odd-parity spin-loop-current order mediated by transverse spin fluctuations in cuprates and related electron systems*, *Phys. Rev. Research* **3**, 013127 (2021).
- [7] S. Onari and H. Kontani, *Origin of diverse nematic orders in Fe-based superconductors: 45 degree rotated nematicity in AFe_2As_2 ($A = \text{Cs}, \text{Rb}$)*, *Phys. Rev. B* **100**, 020507(R) (2019).
- [8] R. Tazai, Y. Yamakawa and H. Kontani, *Charge-loop current order and Z3 nematicity mediated by bond-order fluctuations in kagome metals*, *Nat. Commun.* **14**, 7845 (2023).
- [9] J. M. Luttinger and J. C. Ward, *Ground-State Energy of a Many-Fermion System. II*, *Phys. Rev.* **118**, 1417 (1960).
- [10] H. Li, S. Cheng, B. R. Ortiz, H. Tan, D. Werhahn, K. Zeng, D. Johrendt, B. Yan, Z. Wang, S. D. Wilson, and I. Zeljkovic, *Electronic nematicity in the absence of charge density waves in a new titanium-based kagome metal*, *Nat. Phys.* **19**, 1591 (2023).
- [11] H. Yang, Y. Ye, Z. Zhao, J. Liu, X.-W. Yi, Y. Zhang, J. Shi, J.-Y. You, Z. Huang, B. Wang, J. Wang, H. Guo, X. Lin, C. Shen, W. Zhou, H. Chen, X. Dong, G. Su, Z. Wang, H.-J. Gao, *Superconductivity and orbital-selective nematic order in a new titanium-based kagome metal CsTi_3Bi_5* , arXiv:2211.12264.
- [12] H. Kontani, R. Tazai, Y. Yamakawa, and S. Onari, *Unconventional density waves and superconductivities in Fe-based superconductors and other strongly correlated electron systems*, *Adv. Phys.* **70**, 355 (2021).